AGU PUBLICATIONS

JGR

Journal of Geophysical Research: Solid Earth

RESEARCH ARTICLE
10.1002/2017JB014218

Key Points:
- The physics of crystal-rich systems is rationalized by the introduction of hydrogranular mechanics based on the occurrence of force chains
- A discrete element model of magma dynamics is used to exemplify the contact and force microstructure using anisotropy tensors
- The Sommerfeld and viscous numbers are introduced to discriminate dynamic regimes and modes of mechanical jamming

Supporting Information:
- Supporting Information S1
- Movie S1

Correspondence to:
G. W. Bergantz,
bergantz@uw.edu

Citation:
Bergantz, G. W., J. M. Schleicher, and A. Burgisser (2017), On the kinematics and dynamics of crystal-rich systems, *J. Geophys. Res. Solid Earth*, *122*, doi:10.1002/2017JB014218.

Received 17 MAR 2017
Accepted 14 JUL 2017
Accepted article online 18 JUL 2017

On the kinematics and dynamics of crystal-rich systems

George W. Bergantz[1], Jillian M. Schleicher[1], and Alain Burgisser[2]

[1]Department of Earth and Space Sciences, University of Washington, Seattle, Washington, USA, [2]Institut des Sciences de la Terre, CNRS–IRD–Université de Savoie, Campus Scientifique, Le Bourget du Lac, France

Abstract Partially molten rocks, often called a mush, are examples of a hydrogranular mixture where the dynamics are controlled by both fluid and crystal-crystal interactions. An obstacle to progress in understanding high-temperature hydrogranular systems has been the lack of adequate levels of description of microphysical processes. Here we rationalize the hydrogranular kinematic and dynamic states by applying the concept of particle (crystal) force chains. We exemplify this with discrete-element computational fluid dynamic simulations of the intrusion of a basaltic melt into an olivine-basalt mush, where crystal-scale force chains, crystal transport, and melt mixing are resolved. To describe the microscale kinematics of the system, we introduce the coordination number and the fabric tensors of particle contacts and forces. We quantify the changing contact and force fabric anisotropy, coaxiality, and the connectedness of the mush, under dynamic conditions. To describe the dynamics, particle and fluid characteristic response times are derived. These are used to define local and bulk Stokes numbers, and viscous and inertia numbers, which quantify the multiphase coupling under crystal-rich conditions. We employ the Sommerfeld number, which describes the importance of crystal-melt lubrication, with a viscous number to illustrate the dynamic regimes of crystal-rich magmas. We show that the notion of mechanical "lock up" is not uniquely identified with a particular crystal volume fraction and that distinct mechanical behaviors can emerge simultaneously within a crystal-rich system. We also posit that this framework describes magmatic fabrics and processes which "unlock" a crystal mush prior to eruption or mixing.

"*We cannot define something except in terms of ideas already at our disposal…*"

-Clifford Ambrose Truesdell III [1980]

1. Introduction

There is controversy about the duration, dynamics, and physical conditions of magmatic systems [*Adam et al.*, 2016; *Barboni et al.*, 2016; *Cooper and Kent*, 2014; *Rubin et al.*, 2017]. Conflicting geological, geochemical, and geophysical evidence suggest that magmas and migmatites are either short-lived or can persist in a crystal-rich state for time spans up to 10^6 years [*Barboni et al.*, 2016; *de Silva and Gregg*, 2014; *Kaiser et al.*, 2017; *Paterson et al.*, 2016; *Pritchard and Gregg*, 2016; *Stelten et al.*, 2017; *Ward et al.*, 2014]. In the plutonic record this is often expressed as complex time-transgressive mineral and magnetic fabrics with evidence for both fluid and granular (crystal-crystal) interactions [*Collins et al.*, 2006; *Gutiérrez et al.*, 2013; *Holness et al.*, 2007; *Jerram et al.*, 2003; *Nicolas*, 1992; *Paterson*, 2009; *Sawyer*, 2008] and in the volcanic record by the eruption of crystal-rich magmas with a complex crystal cargo [*Bachmann et al.*, 2002; *Charlier et al.*, 2007; *Klemetti and Clynne*, 2014; *Lindsay et al.*, 2001; *Thomson and Maclennan*, 2013] (see Figure 1). Persistent crystal-rich conditions in basaltic magma bodies have also been inferred based on seismic evidence from ocean islands and mid-ocean ridges [*Lin et al.*, 2014; *Sinton and Detrick*, 1992] and by the occurrence of picrites [*Rhodes*, 1995]. Collectively, these observations have been rationalized with the hypotheses that they are a crystal-rich mush, waxing and waning in response to open-system input and cooling. A corollary to this so-called "mush model" for magma systems is that interstitial melt can be extracted to produce crystal-poor evolved magmas [*Allan et al.*, 2017; *Bachmann and Bergantz*, 2004, 2008; *Hildreth*, 2004], a process already documented in migmatites [*Brown*, 1994]. However, the physical mechanisms of crystal-rich mixing and melt extraction from magmatic and migmatitic crystal-rich systems are complex and poorly understood [*Brown*, 2004; *Brown et al.*, 1995], and the simple application of notions like crystal settling and compaction is not always in agreement with the diversity of complex natural examples [*McBirney et al.*, 2009; *Walker et al.*, 2015] or experimental results [*Schmidt et al.*, 2012]. This reflects the contributions from both buoyancy and deformation-assisted reorganization of crystal-rich systems, which are often punctuated by open-system events.

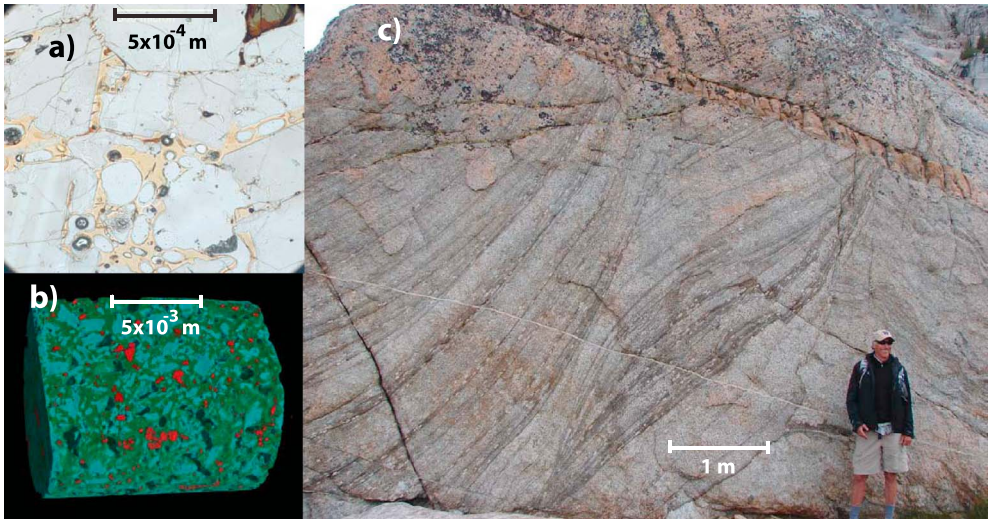

Figure 1. Examples of hydrogranular behavior from the crystal to the outcrop scale, over 5 orders of magnitude. (a) Melt-present cumulate gabbro xenolith where vesiculated brown glass occupies intergranular pores and grain edges [*Bercovici et al*., 2016]. (b) 3-D rendering of a computational tomography image of lava from Llaima volcano, Chile. Sample is ~1.2 cm long and contains ~40 vol % crystal on a vesicle-free basis. Glass is green, and crystals are mostly millimeter-sized olivine (red) and plagioclase (cyan). (c) Crystal-rich gravity currents form schlieren-bounded troughs with strong mineral alignment fabric, Sawmill Canyon, eastern margin of the Tuolumne Batholith, central Sierra Nevada, California [*Paterson et al*., 2008; *Solgadi and Sawyer*, 2008].

The examples cited above express the diversity of phenomena collectively known as hydrogranular behavior. In our usage, hydrogranular refers to a saturated, mobile, multiphase mixture where pore pressure is everywhere defined and particles (or particle clusters) exchange forces that can be idealized as point contacts and can undergo dilation or compaction upon shearing. Even simple hydrogranular media manifest a remarkable variety of physical states from fluid-like to viscoplastic with dissipation occurring from both granular and hydrodynamic interactions simultaneously. Yet they poorly recover end-member behavior: they are not normal solids since they do not produce uniform lithostatic stress, and they do not necessarily manifest affine behavior when they flow. Hydrogranular media undergo dilation, strain localization, abrupt shear thickening, disassociation, and can manifest phase segregation. Even at low Reynolds number nonaffine behavior breaks the time symmetry of the flow, as demonstrated by a multiphase reframing of Taylor's canonical experiment [*Ness et al*., 2017; *Souzy et al*., 2016]. The challenge in their description is that the length scales required for a stationary average are not obvious; they have a history and emergent behavior [*Bak*, 1996]. Hydrogranular systems are "lumpy," because the ratio of the particle size to system size is much larger compared to simple solids or fluids, where properties can be represented by conditions at a point of vanishing size [*Haff*, 1983]. Hence, the physical description of a hydrogranular mixture takes special care, as granular interactions are inelastic and dissipate energy over a much smaller length scale than simple fluids. And any process that produces local segregation can lead to metastable, nonequilibrium "unmixing" of a multiphase system such that one cannot predict in advance the phase distributions and their microstructures from initial conditions or global length scales.

Previous efforts at describing nondilute multiphase flow under high-temperature conditions have relied almost exclusively on the assumption that distinct hydrodynamic and granular modes of dissipation can be adequately averaged through the notion of a suspension viscosity. This is typically augmented by a reference state such as a strength threshold or "lock up" [*Marsh*, 1981]. While these early efforts were novel and inspired by an insightful assessment of natural examples, subsequent work has not yielded a convergence to a widely applicable set of continuum closures [*Petford*, 2009], as lab and numerical experimental results reveal a strong sensitivity to crystal fraction and orientation [*Hoover et al*., 2001; *Martin et al*., 2006; *Philpotts et al*., 1999; *Philpotts et al*., 1998; *Saar et al*., 2001]. Conventional suspension rheology does not explicitly predict or resolve the emergence of first and second normal stress differences, which signals the onset of frictional interactions and dilatational strain. The obstacle is that it relies on averaged volume fractions (or porosity) as the dominant state variable, sometimes the *only* state variable. The purpose of this

work is to introduce and exemplify additional levels of description of hydrogranular interactions in crystal-rich systems, as a first step in linking the characterization of multiphase behavior under dilute conditions by *Burgisser et al*. [2005] with the crystal-rich state.

In closing the Introduction, we direct an interested reader to a brief review of the historical development of ideas that are emphasized in this work. *Campbell* [2006] (quoting citation in *Duran* [2000]) points out that Titus Lucretius Carus (~98–55 B.C.) noticed that a granular solid can flow like a liquid, "One can scoop up poppy seeds with a ladle as easily as if they were water and, when dripping the ladle, the seeds flow in a continuous stream." The mechanical description of natural materials as a granular assemblage was attempted by Couplet in 1727, 49 years before Coulomb's influential work on "earth pressure" [1776] which disregarded the discrete nature of particulate materials [*Terzaghi*, 1920]. There was little subsequent progress in the physics of granular materials with the important exceptions of establishing that granular packings are not hydrostatic by Huber-Burnand in 1829 (and described more fully by Janssen in 1895) [*Sperl*, 2006], the model for contact dynamics of *Hertz* [1882], and the description of dilatancy by *Reynolds* [1885]. *Terzaghi* [1920] noted the limitations in Coulomb's approach but found a first principles description of granular media unwieldly and resorted to experiments to explore the average behavior of soil. *Smith et al*. [1929] attempted to relate the porosity to the number of particles in contact but did not find a way to assess the magnitude of the forces carried by individual contacts. R. A. Bagnold produced seminal work on granular flows, proposing a "grain inertia regime" where the stresses depend on the square of the shear rate [*Bagnold*, 1941, 1954]. *Casagrande and Carrillo* [1944] observed that soil samples under loading had both an inherent and induced anisotropy but did not identify the origins of that behavior. The use of photoelastic discs provided a novel means to finally observe the nature of force transmission in particulate assemblages and confirmed that it was nonhydrostatic and skeletal [*Dantu*, 1957; *de Jong and Verruijt*, 1969; *Oda and Konishi*, 1974; *Wakabayashi*, 1950]. *Biarez and Wiendieck* [1963] introduced the important notion of the coefficient of fabric normal anisotropy, and *Satake and Cowin* [1978] demonstrated that the normal contact distribution could be described by a second-order anisotropy tensor. Perhaps the most significant development in the twentieth century was the advent of the computational tool of the discrete element method (DEM) based on contact mechanics [*Cundall and Strack*, 1979]. This allowed for numerical experiments to probe the micromechanics of particulate mixtures in unprecedented detail, which produced an explosion of new work, much of which is summarized in a number of (recommended) texts and review papers [*Andreotti et al*., 2013; *Campbell*, 2006; *Delannay et al*., 2017; *Duran*, 2000; *Forterre and Pouliquen*, 2008; *Franklin and Shattuck*, 2015; *Iverson*, 1997; *Meier et al*., 2007; *Oda and Iwashita*, 1999; *Vermeer et al*., 2004].

2. Numerical Experiments of Hydrogranular Processes

To develop and exemplify some relevant concepts of hydrogranular processes, we employ our previously published discrete element method (DEM) simulations [*Bergantz et al*., 2015; *Schleicher et al*., 2016] (please see Text S1 in the supporting information for a full elaboration of the theory and numerical implementation and Movie S1 in the supporting information), the nomenclature is defined in Table 1. None of these previous works have described the stresses and corresponding microstructures as we do here. Briefly, the DEM method combines a Eulerian representation of the conservation of mass and momentum balance for the fluid phase, and the motion of a particle of mass m is explicitly solved as a Lagrangian quantity,

$$m\frac{d}{dt}\begin{pmatrix}\mathbf{v}\\ \boldsymbol{\omega}\end{pmatrix}=\sum\begin{pmatrix}\mathbf{F}\\ \boldsymbol{\Gamma}\end{pmatrix} \tag{1}$$

where t is time and with translational velocity vector $\mathbf{v}$ and rotational velocity vector $\boldsymbol{\omega}$ subject to force vector $\mathbf{F}$ and torque vector $\boldsymbol{\Gamma}$. Our application of the DEM method explicitly resolves particle sustained frictional contact, collisions, buoyancy, hydrodynamic drag, interphase momentum transfer, and implicitly treats lubrication; additional information regarding the governing equations and the verification and validation procedures are in the supporting information and can be found in *Garg et al*. [2012a, 2012b] and *Li et al*. [2012]. The fluid phase is modeled with the usual Navier-Stokes equation on a cell size that is approximately 2.5 particle diameters.

The model system is an olivine-rich magma and is shown in Figure 2; the theory, governing equations, validation protocols, and simulation parameters are given in the supporting information and Table S1 in

Table 1. Symbols and Parameters Defined

Symbol	Definition
a_c a_N	contact and normal force anisotropy index
C	number of particle contacts
C	constant in Blake-Kozeny-Carmen relationship
D	particle diameter
$\mathbf{F}_c$, $\mathbf{F}_n$	contact and normal force tensors
H_o	mush thickness
I, I_{vg}, I_{vP}, I_{Iff}, I_{IP}	inertia numbers: generic, gravity forcing, pressure forcing, gravity free-fall, pressure free-fall
k	permeability
m	particle mass
$\mathbf{n}$, N	particle contact normal, number of contacts
P	pressure
s	Sommerfeld number
St, St_B	Stokes number, Stokes number based on bulk shear rate
t, t^*	time, dimensionless time
U_o	velocity of incoming magma
v, v_p, v_f	particle relative velocity, particle velocity, fluid velocity
Z	coordination number
α, α_I	constant in Blake-Kozney-Carman law, constant in friction law
ρ_p, ρ_f	particle and fluid density
η_f	fluid dynamic viscosity
δ, δ_{rough}	particle gap, particle roughness scale
σ_N	particle normal force in lubrication calculation
ϕ, ϕ_{RCP}, ϕ_{RLP}, ϕ_{pc}	particle volume fraction, particle random close packing, particle random loose packing, critical particle volume fraction
$\mu(I)$	friction law
γ	shear rate
τ_{micro}, τ_{macro}	local (Lagrangian) and far-field (Eulerian) characteristic time scales

the supporting information. The domain is 2.56 × 1.28 m and initialized with particles (olivine crystals) that have been allowed to settle forming a bed within a fluid (magma)-filled reservoir. The reservoir and the pore space are filled by basaltic melt colored black, giving an average fluid-volume fraction in the bed of ~0.4, approximating random loose packing. The olivine is colored with horizontal stripes as an aid in visualization; however, all crystals have the same properties as given in Table S1. New crystal-free basaltic magma is injected into the domain from the base and is colored white, and mixing between it and the resident melt is shown as a gradient from black to white. Conservation of mass and pressure relief is provided by mass flow through the upper boundary. Solid boundaries have a no-slip boundary condition for the fluid and a wall-friction law for the crystals, but the majority of fluid and particle motion occurs far from the walls, so boundary conditions have little influence on the dynamics. Since our purpose is to exemplify concepts from hydrogranular kinematics and dynamics, rather than develop a fully geologically realistic scenario, our domain is quasi-two-dimensional. In the context of discrete element models that means that the system is only one crystal wide. However, all the elements of description of the microstructure and methods of characterization can be directly extended to three dimensions with no loss of generality.

Figure 2 shows four time steps in the numerical experiment. Figure 2a shows the initial condition of a static bed. Figure 2b is the corresponding initial condition, but where the particle normal forces are identified and colored by whether they have greater than the instantaneous mean force (red) or less than the mean force (blue). We use the instantaneous mean, rather than a fixed mean, of all the normal forces to better illustrate the fluctuating character of the normal forces. Note that the normal force distribution forms a skeletal or thread-like pattern, which is a manifestation of what are considered to be force chains (described below). The dimensionless time is given for each time step in the top right-hand corner of Figures 2a, 2c, 2e, and 2g. Dimensionless time is defined as

$$t^* = \left(\frac{U_0}{H_0}\right) t \tag{2}$$

where U_0 is the velocity of the incoming crystal-free magma and H_0 is the thickness of the mush. The fluid mechanics and mixing associated with this process have been described elsewhere [*Bergantz et al.*, 2015;

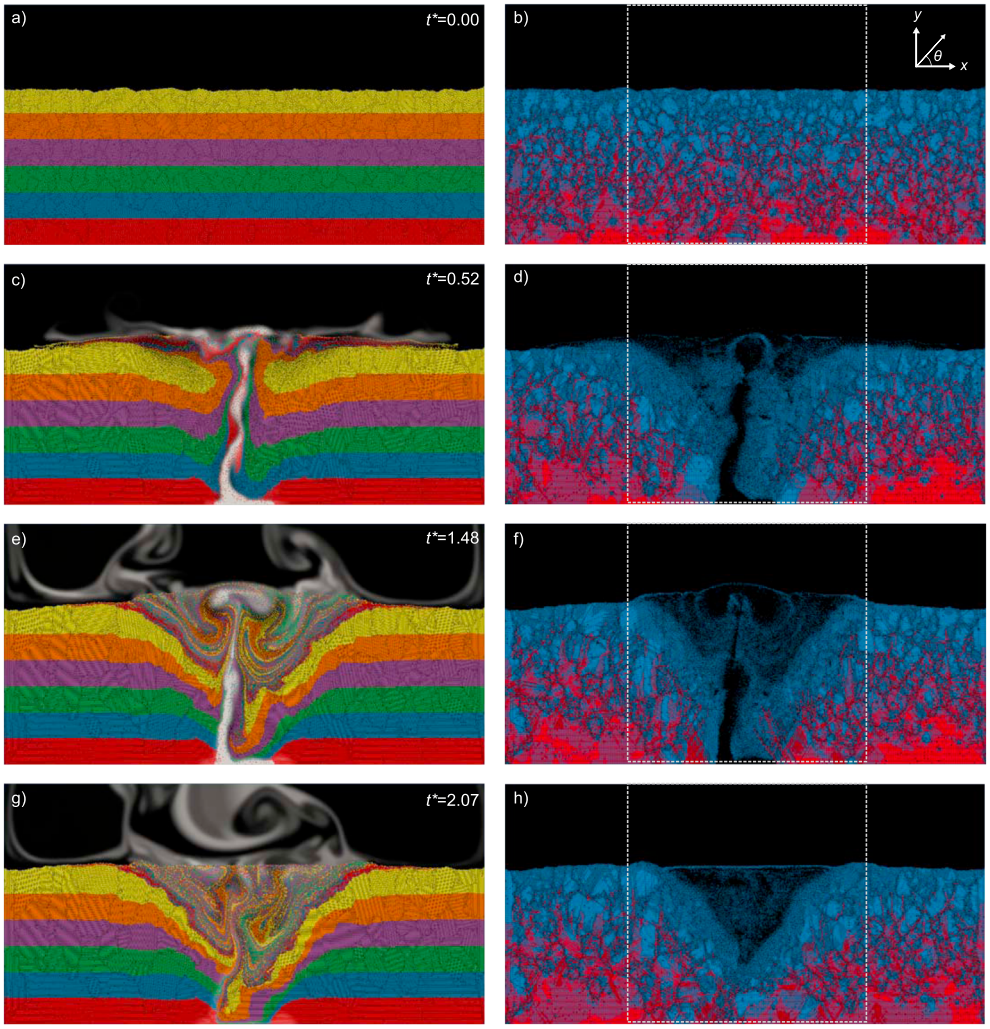

Figure 2. Four time steps of the discrete element simulation of basaltic melt intruding a basalt mush, and the corresponding particle normal forces. Domain is 2.56 × 1.28 m. (a, c, e, and g) The progress of mush fluidization and crystal mixing and (b, d, f, and h) the corresponding normal forces between the particles. Normal forces colored red have larger than the mean force, and those in blue carry less than the mean force. The mean force is calculated over the entire domain at every time step and varies between 1% and 10%. See text for discussion and Movie S1 for a full animation. Details of the calculation are found in the supporting information [*Alizadeh et al.*, 2014; *Coetzee and Els*, 2009; *Cole and Hopkins*, 2016; *Costa et al.*, 2010; *Davidson et al.*, 2001; *Li and Guenther*, 2012; *Nakamura and Watano*, 2007; *Paulick et al.*, 2015; *Peng et al.*, 2014; *Richter et al.*, 2003; *Ruprecht et al.*, 2012; *Tsuji et al.*, 1993; *Wallace and Bergantz*, 2005].

Schleicher et al., 2016]; our focus here is on the hydrogranular microphysics. The input of new magma is held steady until $t^* = 1.65$ at which time it is shut-off and the fluidized magma collapses. Figures 2g and 2e illustrate the process of collapse at $t^* = 2.07$, well after the shut-off has occurred, please see Movie S1.

3. Kinematics of Hydrogranular Media

Here we consider some of the characteristic features of hydrogranular media with an emphasis on crystal-rich conditions.

3.1. Force Chains

The skeletal, nonhydrostatic distribution of force on a scale larger than the particle size was firmly established by experiments with optically sensitive discs [*Behringer et al.*, 1999; *Dantu*, 1957; *de Jong and Verruijt*, 1969], 3-D X-ray diffraction [*Hurley et al.*, 2016], and later DEM numerical experiments [*Cundall and Strack*, 1983]. These observations were rationalized with the notion of "force chains" [*Antony*, 2007] as illustrated in Figure 3. While there is no singular definition of a force chain, it is generally understood as being a

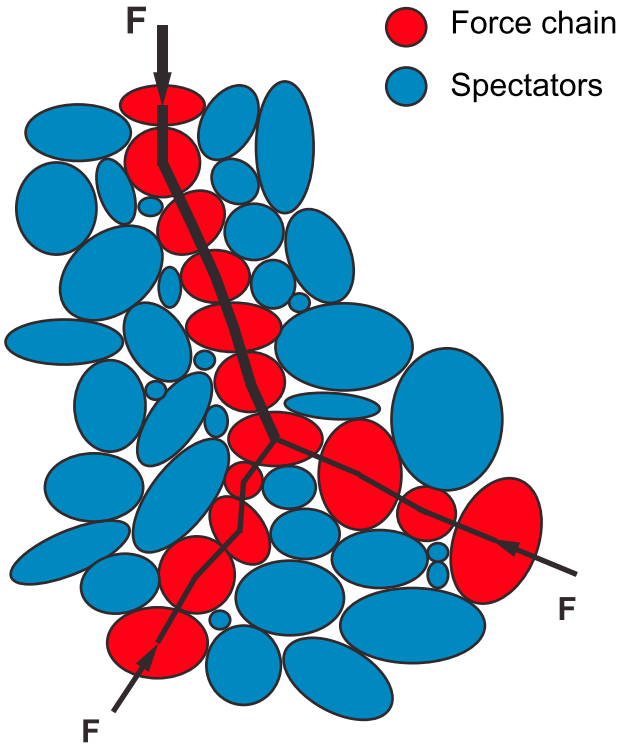

Figure 3. Schematic of particles under some load, with the resulting force chain. Force chain branching and the discrete nature of force distribution are illustrated. The blue particles are so-called spectators in that they carry less than the mean force.

colinear arrangement of at least three particles carrying more than the mean force, and typically has a length of up to 10 particles. [*Cates et al*., 1998; *Guo*, 2012; *Muthuswamy and Tordesillas*, 2006; *Peters et al*., 2005; *Wambaugh*, 2010]. The fundamental topology of a force chain is that it typically branches, forming arches, and transmitting force oriented around some mean at the macroscale. To quantify force propagation in granular systems, particle arrangements can be idealized as shown in Figure 4, where two particles A and B are in contact. The contact normals are given by n_{AB} and n_{BA}, the force vectors at the point of contact by f_{AB} and f_{BA}. The branch vector is defined as a line connecting the fixed centroid of the particles, which for spherical particles is the sum of d_{BA} and d_{AB}, but in nonspherical particles (see section 5) the radius is not uniquely defined and the branch vector dimension can change as particles translate and rotate.

Importantly, the distribution of forces in a quasi-static hydrogranular media has a bimodal character [*Majmudar and Behringer*, 2005; *Radjai et al*., 1998] with a strong network parallel to the loading and a weak load-carrying network that is isotropic or slightly perpendicular to the loading, acting as a type of "pressure." This is shown in Figures 2b, 2d, 2f, and 2h, where the normal forces with greater than the instantaneous average force are shown in red and those with less than the average force are shown in blue. These can be seen to be forming a fluctuating skeletal network of particles with greater than the mean force distributed quasi-linearly across many particles. These are force chains. Figure 5 shows a circular probability density function of particle contact normals colored as in Figure 2 (see Figure 2b), and the corresponding probability density distributions of the forces are shown, normalized to the mean force, that correspond to the time step in Figures 2a and 2b. The distribution in Figure 5 is like that encountered in other studies, where the strong network is 40% or less of the total number of contacts and has an exponential distribution, and the weak network a power law distribution [*Radjai et al*., 1996; *Radjai et al*., 1998], confirming that a simple model of sedimentation and cumulate formation in a magma body can produce a crystal mush that can be described as a hydrogranular system. Note that in Figure 5a there is a clear anisotropy to the orientation of the

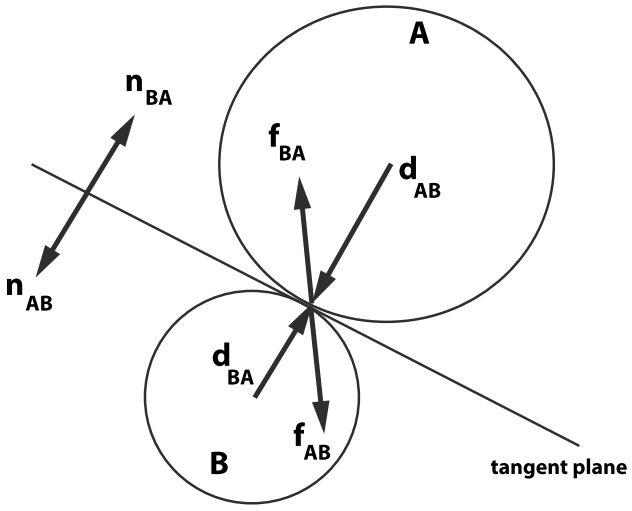

Figure 4. Nomenclature for an idealized system of particle contacts between two particles A and B for use in the calculation of the microstructure.

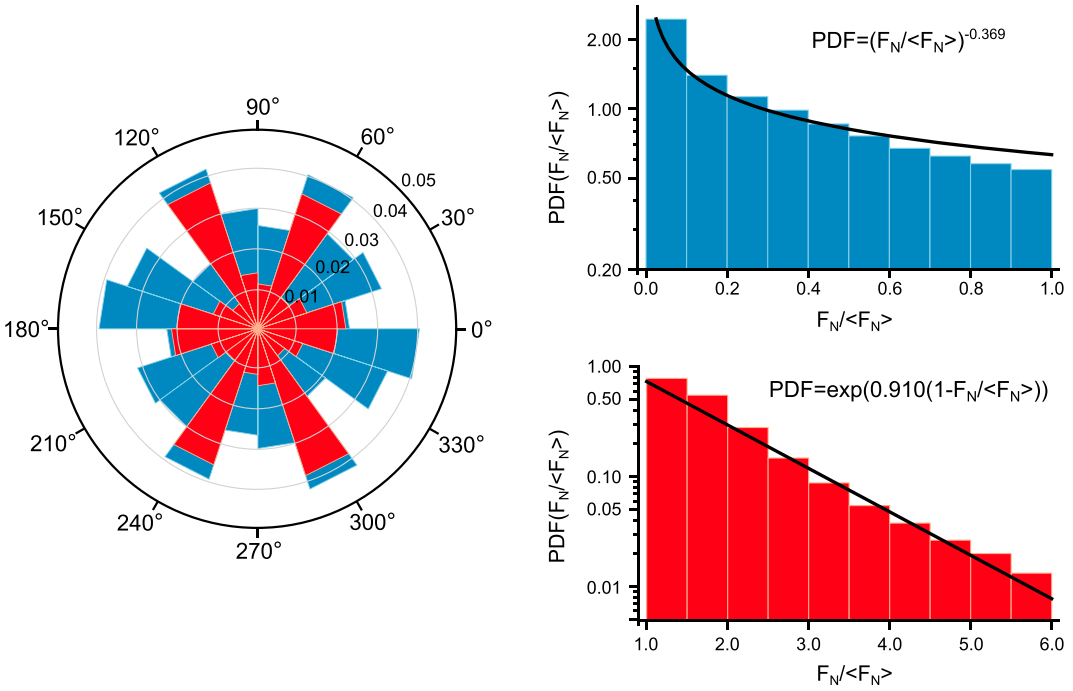

Figure 5. Spatial distribution of normal forces from Figures 2a and 2b which represent the initial condition. Data are taken from the region in Figure 2b within the central white box. The colors are same as that in Figure 2b, where the red forces carrying the mean or more than the mean and the blue less than the mean.

load-bearing contact normals, while the more numerous contacts carrying less than the mean force are more uniformly distributed; this will be discussed in detail below.

The lowest level of description of a hydrogranular media is the particle contact density function, $\xi(c)$, which is defined as the proportion of particles with an integer number of contacts, c. The coordination number, Z, is the average number of particle-particle contacts per particle throughout the granular system.

$$Z = \sum_{c} c\xi(c) \tag{3}$$

As a granular media is assembled, the number and distribution of the particle contacts are conditioned by steric (excluded volume) constraints that produce angular exclusions at an angle of about $\pi/3$ for a unimodal distribution. The occurrence of particle exclusion controls the initial dilatancy, coordination number, permeability, and hence pore pressure transmission and dissipation [*Madadi et al*., 2004; *Radjai et al*., 2012]. This leads to an initial sensitivity in strength and encodes the granular framework with a history [*Vanel et al*., 1999] and an anisotropic structural bias.

A consequence of this is that a static granular media is not a simple elastic body since a change in shear orientation can induce a reorganization of the media with dissipation, and local reversibility is not necessarily achieved [*Ness et al*., 2017]. This produces a plastic condition called "fragility" that has a dual nature, a microfragile rapid strain response associated with initial contact breakage, followed by a macrofragile structural response associated with local reconfiguration of the granular media where there is nothing to enforce a spatial or temporal symmetry [*Cates et al*., 1998; *Ness and Sun*, 2016b; *Ness et al*., 2017]. Hence, strength is not uniquely and universally defined, as incremental increases in loading can lead to a macrofragile reconfiguration of granular elements such that a new (nonreversible) marginal equilibrium load-bearing state is achieved [*Cates et al*., 1998], a result anticipated but not completely clarified by *Wildemuth and Williams* [1984, 1985] and *Kanai et al*. [1992]. During deformation the force chains migrate as percolating networks on a time scale approximately the inverse of the shear rate, where force is discontinuously transmitted by abandoning existing force chains and the recruitment of particles that were previously spectators into new chains, with the continuous rotation of the branch vectors (see Figures 2 and 3). In the quasi-static regime this process is

phenomenologically a buckling of the force chain [*Cundall and Strack*, 1983; *Guo*, 2012; *Tordesillas*, 2007; *Tordesillas et al*., 2014; *Tordesillas et al*., 2009]. However, for this buckling to occur it requires a rearrangement of particles in the region surrounding the force chain, as controlled by the interplay between steric constraints and the local void ratio. This produces what is termed a "nonlocal" condition where displacements require mutual interactions over some length or volume scale that is a multiple of the particle diameter and a function of the properties of the far-field granular media. The implication of this is that shear rate depends not only on shear stress but also the degree of mobility in the surroundings [*Bouzid et al*., 2015a; *Bouzid et al*., 2013, 2015b; *Mansard and Colin*, 2012]. This nonlocal behavior produces shear banding and strain localization, nonuniform dilation, stick-slip behavior, and nonaffine deformation that yields a noncontinuum condition [*Tordesillas*, 2007].

3.2. Microstructure: Fabric Tensors and Anisotropy

Hydrogranular systems are inherently anisotropic in the sense that the orientations of applied boundary forces are not transmitted uniformly throughout the media, as force chains locally branch and redirect around some mean value. This poses challenges for the description of granular materials as a (plastic) continuum, where the usual assumption of stress and strain coaxiality is required to formulate the constitutive closures [*Hill*, 1950]. Noncoaxiality between contact or shape, and force, normals arises through interactions involving grain-scale properties such as variable shape and friction [*Ai et al*., 2014; *Jiang et al*., 2017; *Zhao and Guo*, 2015], perhaps similar to noncoaxiality observed in simulations of melt-present processes in the Earth's mantle with viscosity heterogeneity [*Butler*, 2012; *Katz et al*., 2006]. To quantify this anisotropy, a description of the microstructure is required.

Collectively, microstructure refers to the orientation of the particle contacts (normals), the distributions of forces among those normals, the branch vector orientations which connect particle centers (in nonspherical cases), and the particle shape primary axis orientation when combined with the coordination number (see Figure 4). These elements comprise the so-called fabric of the hydrogranular media, expressed as tensor state variables and can be extended to polydisperse granular systems [*Madadi et al*., 2004]. Note, however, that while any probability density function (PDF) of a microstructural element can yield a fabric tensor, a fabric tensor does not yield a unique PDF, This level of description was developed to describe geological examples [*Curray*, 1956; *Friedman*, 1965; *Gipson*, 1965; *Laird*, 1970] and soil [*Brewer*, 1964; *Oda*, 1972], and the fabric tensor can be mapped to a directional PDF as exemplified in Figure 6 below [*Bathurst and Rothenburg*, 1990; *Oda et al*., 1985; *Rothenburg and Bathurst*, 1989]. The fabric tensor represents the average of the n unit vectors over all particles and can be weighted to express either force magnitude or a particle shape orientation.

For the contact normals, the tensor $\mathbf{F}_c$ is constructed by the spatial integration of the directional probability density function $E(\mathbf{n})$ over N contacts where $\otimes$ is the tensor product

$$\mathbf{F}_c = \oint_{\Omega} E(\mathbf{n})\mathbf{n}\otimes\mathbf{n}d\Omega = \frac{1}{N}\sum_{k=1}^{N} n^k \otimes n^k \tag{4}$$

which for the two-dimensional case considered here with a Cartesian coordinate system (see coordinate reference frame inset in Figure 2b), $E(\mathrm{n})$ can be written as $E(\theta)$ which produces a symmetric second rank tensor of trace unity

$$F_{ij} = \frac{1}{N}\begin{bmatrix} \sum_{k=1}^{N}\cos\theta^k\cos\theta^k & \sum_{k=1}^{N}\cos\theta^k\sin\theta^k \\ \sum_{k=1}^{N}\sin\theta^k\cos\theta^k & \sum_{k=1}^{N}\sin\theta^k\sin\theta^k \end{bmatrix} \tag{5}$$

The eigenvalues of the tensor are given by

$$\begin{matrix} F_1 \\ F_2 \end{matrix} = \frac{F_{11}+F_{22}}{2} \pm \sqrt{\frac{(F_{11}-F_{22})^2 + 4F_{12}F_{21}}{2}} \tag{6}$$

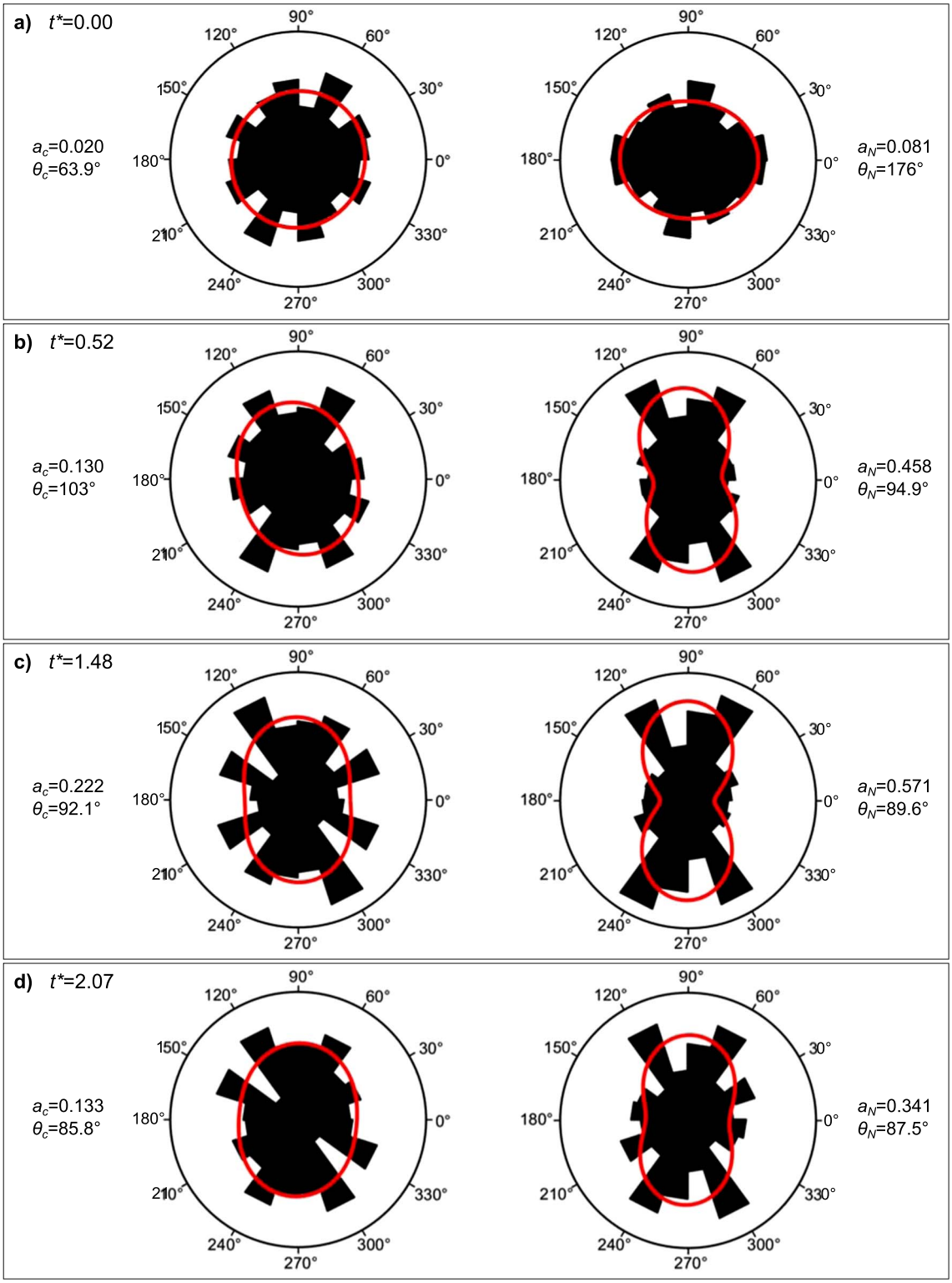

Figure 6. The circular distributions (probability density functions or PDFs) for both the contact and force microstructures from the area enclosed in the white box in Figure 2b are shown. (a–d) The four time steps shown in Figure 2. The red curve is the fit to the PDFs based on (9) and (11).

The fabric tensor given by (5) has two degrees of freedom represented by scalar values a_c and θ_c, where an anisotropy index can be defined as

$$a_c = 2\frac{F_1 - F_2}{F_1 + F_2} \tag{7}$$

where a_c is the deviatoric invariant, or the anisotropy intensity factor, or the coefficient of variation of F_{ij} and a value of zero indicates an isotropic condition such that contact normals are uniformly distributed in an angular PDF. The principal direction which is the eigenvector orientation of F_{ij} corresponding to the larger eigenvalue is given as

$$\theta_c = \frac{1}{2}\arctan\left(\frac{F_{12} + F_{21}}{F_{11} - F_{22}}\right) = \frac{1}{2}\arctan\frac{\sum_{k=1}^{N}\sin 2\theta^k}{\sum_{k=1}^{N}\cos 2\theta^k}. \tag{8}$$

where θ_c is the mean. Since $E(\theta)$ is a periodic function in θ it can be expanded as a Fourier series as

$$E(\theta) = \frac{1}{2\pi}\{1 + a_c\cos 2(\pi\theta - \theta_c)\}, \tag{9}$$

where a second-order expansion has been shown to be sufficient in representing the distribution and takes a value of $1/2\pi$ in isotropic conditions. In three-dimensional situations the contact fabric tensor $E(\mathbf{n})$ would be described with spherical angles and the Fourier expansion in equation (9) would be replaced by spherical harmonics, and it should be noted that even if the second rank tensor is symmetric, it is generally not true that higher-order tensor products such as the fourth or sixth rank tensors will be [*Kanatani*, 1984].

For describing the distribution of some property in the microstructure such as the magnitude of normal force associated with the contact, a weighting function, I, operating on the unit normal vectors is introduced,

$$\mathbf{F}_N = \int_I \oint_\Omega IE(\pi\mathbf{n}, I)\mathbf{n}\otimes\mathbf{n}d\Omega dI = \frac{1}{N\langle I^k\rangle}\sum_{k=1}^{N} I^k\mathbf{n}^k\otimes\mathbf{n}^k \tag{10}$$

where $\langle I^k\rangle$ is the average of I over k and expressing the distribution as a Fourier expansion as before yields,

$$F_N = \langle F_N\rangle\{1 + a_N\cos 2(\theta - \theta_N)\} \tag{11}$$

where

$$\langle F_N\rangle = \int_0^{2\pi}\langle I(\theta)\rangle d\theta \tag{12}$$

The contact and force weighted normals for the four time steps shown in Figures 1b, 1d, 1f, and 1h are shown in Figure 6 for the region within the white box in Figure 2. We choose to examine a fixed region of the simulation as a reference volume, rather than a fixed particle population. This is because we wish to examine all the coupled hydrogranular processes as a time series, and the highly intermittent nature of the particle behavior with particles transitioning between active and rest states, being expelled from the mixing bowl and so on, made identifying a representative particle population a priori rather arbitrary and unwieldly. We also sought to capture the instantaneous force fabric from fluidized to a fully rest state, connected to the boundary where force chains are ultimately anchored. Hence, we elected to employ a representative volume for purposes of demonstration, as it captures the entire range of the fluctuating and quasi-static behavior.

The initial condition at $t^* = 0$ is nearly isotropic, with a slight anisotropy in the vertical direction as loading from gravity is parallel to the coordinate axis. Of course, truly isotropic conditions can never be achieved in discrete media due to steric (excluded volume) effects from particles [*Radjai et al.*, 2012]. The maximum principal stress associated with the fluid thrust from the incoming magma is in coaxial alignment with gravity, so anisotropy quickly develops in the force contact normals as shown in Figure 6c at $t^* = 1.48$. After the input is shut-off at $t^* = 1.65$ and the crystals begin to slump and settle into a bed, the anisotropy starts to diminish as shown by Figure 6d.

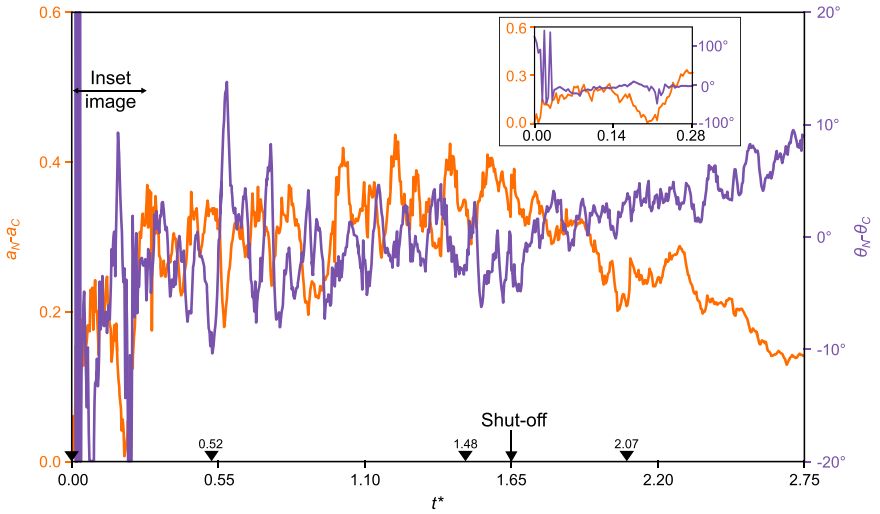

Figure 7. The anisotropy microstructure of the simulation in Figure 2 (area within the white box on Figure 2b) as a function of dimensionless time as given by equation (2). Left axis is the difference between the magnitudes of the force and contact anisotropy, and right axis is the circular PDF of the difference between force and contact distributions. The four panels shown in Figure 2 are called-out on the horizontal time axis at their respective points; the shut-off time for the injection of new magma is shown as well.

The coaxiality between the contact orientations and the force fabrics is presented in Figure 7 using F_c or F_N as appropriate. The left axis is the difference between the magnitudes of the anisotropy of a_c and a_N, both calculated from an equation like (7) for particles within the white frame in Figure 2b, as a function of dimensionless time as given in (2). The right-hand axis is a direct measure of the noncoaxiality as expressed through the difference of θ_N and θ_c. After an initial strongly transient phase associated with the intrusion of the new melt and the disruption of the granular bed, progressive fluidization reduces the number of contacts and force chains are responding to support provided along the hanging wall of the faults that define the steady state fluidized region (we call this region the "mixing bowl" [*Bergantz et al*., 2015]). Once the strong transient has passed, the angular measure of the coaxiality varies over a few degrees. This is not surprising as both the gravity and the new injection are acting in a parallel direction. The "noise" or variability is due to the fact that there is circulation within the fluidized region. One implication of this is that any natural mineral fabric formed under hydrogranular conditions (as opposed to that from grain-boundary processes) there will always be some inherent stochastic bias when looking at the interplay between forces and resulting fabrics under melt-present conditions [*Zhao and Guo*, 2015]. Perfect coaxiality can be approached but never exactly achieved under natural conditions.

Figure 8 shows the coordination number Z and the contact anisotropy a_c as a function of dimensionless time, the four panels from Figure 2 are called-out along the time axis. A near-linear loss of contacts from fluidization finally terminates at about $t^* = 0.275$ which is when the initial input from the newly injected magma finally breaks through and fluidizes the bed. Recall that the idea of fluidization is that support against gravity is provided by hydrodynamic drag, so the value of the coordination number is a measure of the particle "connectedness" in the absence of externally supported force chains in addition to contributions from the quasi-static, but fluctuating, unfluidized region below the mixing bowl. In triaxial tests it has been shown that contacts are gained in the direction of greatest principle stress as force chains grow in number and length with a preferential loss of contacts in the direction of greatest extension [*Rothenburg and Bathurst*, 1989]. This also corresponds to a spike in the contact anisotropy, as there are no longer crowding constraints on the vertical transport. After the injection of new magma is terminated and particles settle individually and as slumps, the support fabric of force chains is reestablished and the coordination number rises accordingly, with a reduction in the contact anisotropy.

As discussed above, the particle contact anisotropy, a_c, is generated by the simultaneous gain of particles in the direction of shortening and loss in the direction of extension. But this simple notion is complicated if there is material transport. In Figure 8, there is a reduction in coordination number but an increase in

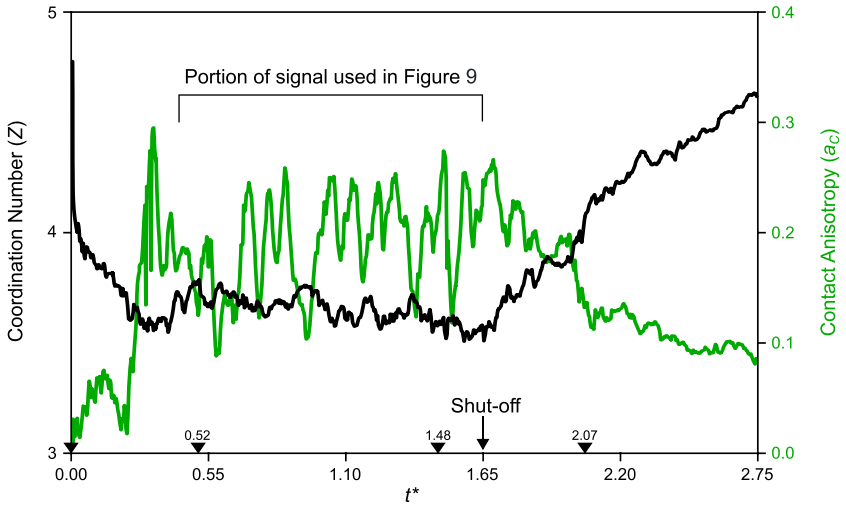

Figure 8. Coordination number, Z, and contact anisotropy index, a_c, as a function of dimensionless time, for the region within the white frame in Figure 2b. The four time steps shown in Figure 2 are identified along the dimensionless time axis as is the shut-off time. During the initial fluidization transient, the coordination number drops as expected, as particle volume fractions are reduced. Once the fluidization has reached a steady state, the coordination number varies around an internally determined value. After shut-off and the collapse of the fluidized region with an associated local increase in particle volume fraction, the coordination number rises as support is reestablished with the subjacent bed.

anisotropy. This can be explained as a result of our initial configuration where gravity and the upward fluidizing input are opposing and collinear. So even though the largest net extensional strain is vertical, that is also the direction of the largest unbalanced principle stress. This yields competing effects: vertical extension lowers the local particle volume fraction and hence coordination number, but of the remaining contacts, there is a vertical bias as gravity and the opposing upward flow drive them together.

Changes in anisotropy associated with nearly constant coordination number during the quasi-steady time of about $t^* = 0.44$ to $t^* = 1.65$, as is evident in Figure 8, are harder to rationalize in that way. If anisotropy is not generated by topological changes in the contact network by contact gain or loss, some other mechanism at nearly constant coordination number must be present. *Kruyt and Rothenburg* [2016] and *Mutabaruka et al.* [2014] propose a second source of dilation and hence changes in a_c by network distortion at constant Z. However, the coordination number and averaged particle volume fraction in our simulations are lower than those studies, especially in the fluidized region, so it is an open question as to whether a distortion mechanism, which implies a sustained contact network, is the explanation.

To assess the relationship between the coordination number and the contact anisotropy, we examined the coherence of their respective time series, in the quasi-steady period from $t^* = 0.44$ to $t^* = 1.65$; the interval is identified on Figure 8. Assuming that a sampling interval of $t^* = 0.003$ provides a stationary (ergodic) record, we detrended each time series to remove any linear bias and dc offsets, and the filtered time series are shown in Figure 9 (top left). Figure 9 (top right)shows the periodogram (power spectral density estimate) for the two time series; most of the power is in the low frequencies so data are shown only to a dimensionless frequency of $f^* = 21.8$. The magnitude-squared coherence of the two periodograms is shown in Figure 9 (bottom)for a larger range of frequencies. But the lack of strong coherence above say, 0.75, indicates that a temporal causation is unlikely (assuming that correlation equals causation). The rapid fluctuations in contact anisotropy as shown in Figure 8 might then be the result of hydrodynamic and pore pressure fluctuations arising from complex behavior within the fluidized region. Consider that the particles used in Figures 4–8 do not come from a uniform kinematic regime (see Figure 10). For example, in Figure 2e, some particles are undergoing large-scale circulation within the "granular vortices" in the upper regions of the mixing bowl, while in the lower regions particles are slumping into the chimney and getting periodically entrained vertically and rapidly transported up the central chimney. Hence, the microstructure is perhaps more conditioned by intermittent fluid process than particle contact-friction until the shut-off is reached.

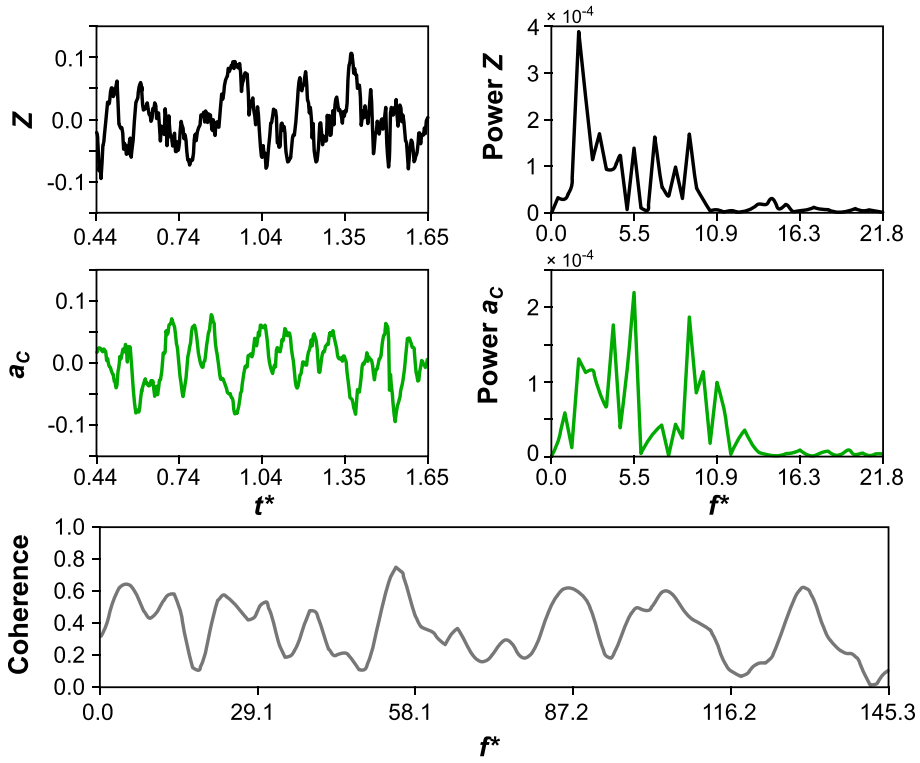

Figure 9. Detrended time series, periodograms, and magnitude-squared coherence for time series of coordination number Z and the contact anisotropy, a_c. See text for discussion.

4. The Dynamics of Hydrogranular Media

The challenge in describing the dynamics of multiphase flow is that there is a multiplicity of coupling and dissipative processes, producing emergent cooperating and competing length and times scales [*Bak*, 1996; *Crowe*, 2006]. One strategy that has been successful in describing dilute flows has been separating the local

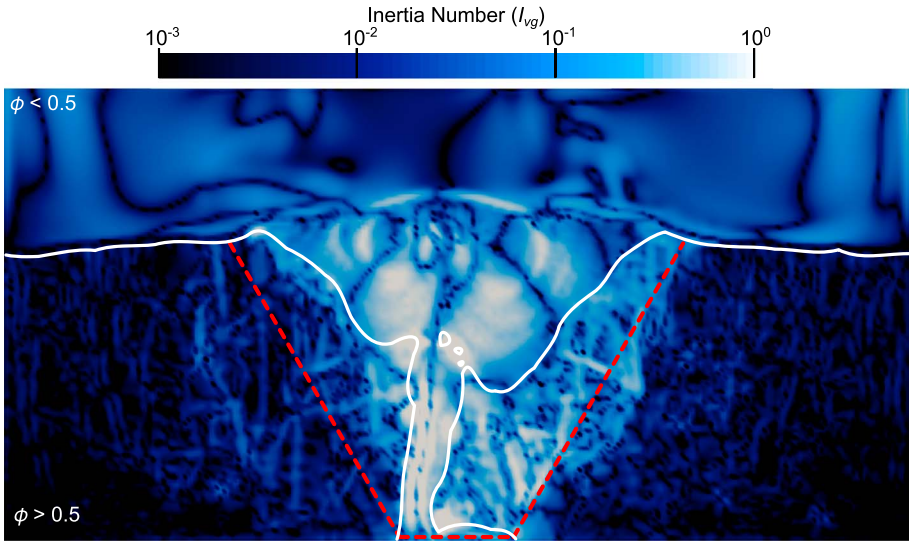

Figure 10. A color contour plot of the viscous number I_{vg}, equation (30), at dimensionless time $t^* = 1.48$, compare with Figures 2e and 2f. The white contour line separates regions with greater or less than a volume fraction of particles of 0.5. The red dashed line is the outline of the mixing bowl. The value of α was calculated with a value of $C = 44$, appropriate for frictionless spheres, and at $\phi \leq 0.304$, α was set to 0.081 to avoid unrealistic values in the very dilute regions where equation (19) does not apply. See text for discussion.

(Lagrangian description) phase behavior of the subordinate phase, such as a crystal, from far-field averaged behavior of the carrier phase, a melt or gas (Eulerian description). For example, one common way to express the momentum coupling is by the dilute Stokes number,

$$St_{\text{dilute}} = \frac{\tau_{\text{micro}}}{\tau_{\text{macro}}} \tag{13}$$

where τ_{micro} is the characteristic response time of a particle subject to a force from the carrier fluid operating over the far-field characteristic time scale τ_{macro} [see *Burgisser et al*., 2005, and references therein]. If this ratio is small, the particle motion is a tracer, completely dictated by that of the bulk fluid, and the system can be treated as a pseudo-single phase material whose properties are described by a weighted average of the phase proportions. If the ratio is very large, the particle and host fluid are not well coupled and the particle acts as a ballistic whose motion can be described independently of that of the fluid. Hence, the Stokes number provides a compact way to identify the extent of the multiphase coupling.

Extending this framework to particle-rich hydrogranular systems is not obvious, as particle-particle interactions can be frictional or collisional, and hydrodynamic forces such as pore pressure and lubrication occur. And importantly, hydrogranular media can undergo a volume change upon shear, manifesting either dilation or compaction [*Modaressi et al*., 1999; *Wroth*, 1958], and strain is accommodated by particles passing over and around each other. However, if the collective behavior of the granular mixture can be considered stationary (in the dynamic sense) by a suitable averaging, it can be described as a "granular continuum" with a characteristic time scale. Conceptually, this granular continuum plays the same role in controlling the macroscopic time scales as the fluid does in the dilute case. And as described in section 3 above, the transmission of force in the hydrogranular mixture depends on the coordination number or the compactness of granular mixture. Hence, any process that acts to dissociate the granular mass, producing particles that decrease their coordination number and become ballistic, is equivalent to a high St_{dilute} for the dilute case. Conversely, processes that act to keep particles in mutual contact are the equivalent to a small St_{dilute} in that the particle follows the bulk granular flow.

4.1. Particle Response Time and Inertia Numbers

To obtain an appropriate form for the particle response time, consider a truncated version of the particle equation of linear motion (1), where the lubrication force is omitted (scale analysis as in *Andreotti et al*. [2013] demonstrates that it only changes the particle response time by a factor of 3):

$$\frac{\pi}{6}\rho_p d^3 \frac{dv_p}{dt} = \frac{\pi}{6}\Delta\rho d^3 g - F_d \tag{14}$$

where v_p is the particle velocity, d is the particle diameter, $\Delta\rho$ is the density difference between particles and fluid, g is the scalar acceleration of gravity, and ρ_p is the particle density. In the absence of fluid drag, F_d, the time scale for a particle to free-fall a distance d is given by

$$\tau_{ff} = \sqrt{\frac{2d\rho_p}{\Delta\,\rho g}} \tag{15}$$

In the case of neutrally buoyant particles or if the particle restoring force is described by a confining pressure, P, acting over the projected particle area instead of gravity,

$$\frac{\pi}{6}\rho_p d^3 \frac{dv_p}{dt} = \frac{\pi}{4}Pd^2 - F_d \tag{16}$$

the free-fall time scale over a distance d is given as

$$\tau_{ff} = d\sqrt{\frac{3\rho_p}{P}} \tag{17}$$

Assuming that the particle Reynolds number, Re_p, is less than unity where

$$\text{Re}_p = \frac{\rho_f d\left|v_p - v_f\right|}{\eta_f} \tag{18}$$

η_f is the fluid viscosity, the drag force can be expressed analytically. If F_d is a simple fluid drag, the information that conditions are dense (i.e., that particles are in close proximity) is lost. Following *Cassar et al*. [2005] we employ a version of F_d that explicitly incorporates the resistance to particle motion associated with the pore pressure generated by the restoring particle having to displace fluid through the adjacent granular media of permeability $k = \alpha d^2$ where α is approximated by the Blake-Kozeny-Carman relationship [*Bachmann and Bergantz*, 2004],

$$\alpha = \frac{(1-\phi)^3}{C\phi^2} \tag{19}$$

where ϕ is the solid volume fraction and C is a constant of order 10^1 to 10^2. There is some uncertainty in the value of α that arises from the fact that the granular framework is not a fixed permeable media and can also deform in response to local pore pressure fluctuations. In particular, this drag is not valid for dilute systems. We set the lower bound of α to 1/12 so as to recover the simple fluid drag (see below). The pressure drop across the projected area is $\eta_f dv_p/k$ producing a drag force,

$$F_d = \frac{\pi}{4\alpha}\eta_f d v_p \tag{20}$$

The solution to (14) with this drag is

$$v_p(t) = \frac{2}{3}\frac{\Delta\ \rho g\ \alpha d^2}{\eta_f}\left[1 - \exp\left(-\frac{3\eta_f}{2\alpha\rho_p d^2}t\right)\right] \tag{21}$$

which for long times becomes

$$v_p(t) = \frac{2\Delta\rho g\alpha d^2}{3\eta_f} = \frac{d}{\tau_{vD}} \tag{22}$$

where the characteristic viscous time scale with pore fluid expulsion modeled by Darcy drag is

$$\tau_{vD} = \frac{3\eta_f}{2\Delta\rho g\alpha d} \tag{23}$$

If instead the fluid drag, F_d, is modeled as simple Stokes flow,

$$F_d = 3\pi\eta_f d v_p \tag{24}$$

The characteristic viscous time scale is given as

$$\tau_{vS} = \frac{18\eta_f}{\Delta\rho g d} \tag{25}$$

The ratio of the two viscous time scales depends critically on the value of α which varies between 0.01 and 0.0001 and suggests that the Darcy drag produces 10 to 1000 times more dissipation than the Stokes drag scaling.

If the restoring force is provided by a confining pressure as in (16) with the Darcy drag (20), the characteristic viscous time scale can be expressed as

$$\tau_{vDP} = \frac{\eta_f}{\alpha P} \tag{26}$$

It is customary in the dense granular physics community to define a Stokes number which is the ratio of the free-fall and fluid drag time scales, expressing the relative contributions of grain inertia and viscous effects in the time scale of the restoring motion. For a gravitational restoring force and a Darcy drag law as in (23) the Stokes number is

$$St_{\text{dense}} = \frac{2\alpha d}{3\eta_f}\sqrt{2dg\rho_p\Delta\rho} \tag{27}$$

It should be noted that the use of the dense Stokes number in (27) is not conceptually the same as the dilute Stokes number defined in (13), as it does not involve the far-field granular media time scale. This macroscopic time scale, τ_{macro}, of the granular media is the inverse of the externally imposed shear rate $\dot{\gamma}$,

$$\tau_{\text{macro}} = \frac{1}{\dot{\gamma}} \tag{28}$$

By combining the two time scales, one for the particle response and one for the bulk granular flow, one can define a quantity called an inertia number, I,

$$I = \tau_{\text{micro}}\, \dot{\gamma} \tag{29}$$

where τ_{micro} can be chosen from the various solutions to equation (14) above. The inertia number serves the same role for dense hydrogranular flows as does the Stokes number for the dilute case as given in equation (13), in that it is a measure of the coupling of a particle to the surrounding granular media undergoing shear. The inertia number was first termed as such for dry granular flows by *da Cruz et al*. [2005] but also developed by dimensional arguments previously [*MiDi*, 2004]. For hydrogranular conditions the inertia number can be decomposed into two contributions, the hydrogranular viscous number which includes both frictional and viscous contributions to the dissipation [*Boyer et al*., 2011; *Ness and Sun*, 2015; *Trulsson et al*., 2012] I_{vg}, where with gravitational forcing and Darcy drag,

$$I_{vg} = \frac{3\eta_f \dot{\gamma}}{2\Delta\rho g \alpha d} \tag{30}$$

or with a confining pressure restoring force and Darcy drag,

$$I_{vP} = \frac{\eta_f \dot{\gamma}}{\alpha P} \tag{31}$$

and an inertia number, associated with the free-fall time scale (15),

$$I_{If} = \dot{\gamma}\sqrt{\frac{2d\rho_p}{\Delta\rho g}} \tag{32}$$

or with an externally applied pressure using (17) in (28),

$$I_{IP} = d\dot{\gamma}\sqrt{\frac{3\rho_p}{P}} \tag{33}$$

4.2. Lubrication Forces

Lubrication refers to the force required for two approaching or diverging particles to squeeze or suck fluid into the gap between them. While usually considered a repulsing force, it can also inhibit particles from being separated (consider the difficulty of drawing a viscous fluid into a syringe). For example, if a hydrogranular framework undergoes a distortion or dilantancy such that there is a local redistribution of the void space, transients in pore pressure will occur. This can have a dual effect—both acting as a local fluidizing agent but also inhibiting phase relative motion as viscous fluid must be drawn into the pore space. This produces an apparent yield strength [*Iverson et al*., 2000; *Pailha et al*., 2008], as observed in the simulations of *Mutabaruka et al*. [2014].

Lubrication forces have slightly different expressions depending on whether particle motion is normal (particles approaching or diverging) or tangential (particles translating past each other). Both expressions, however, share some similarity [*Marzougui et al*., 2015] in that the scaling can be illustrated by the normal forces only. A general form for the normal lubrication force for spheres can be expressed as [*Brenner*, 1961; *Kim and Karrila*, 1991]

$$F_{\text{lub}} = \frac{3\pi\eta_f d^2 \dot{\delta}}{2\left(\delta + \delta_{\text{rough}}\right)} \tag{34}$$

where δ is the width of the gap between particles and δ_{rough} is the characteristic length scale of the particle surface roughness. Although lubrication is present in any particle-fluid multiphase flow it is rarely treated explicitly in dilute flows, such as dilute pyroclastic flows where the viscosity is low, the particle relative velocity is high, and sustained frictional contact infrequent. Under these conditions collisions are the dominant means of particle-particle energy dissipation (expressed as a "granular temperature") and the lubrication force is not explicitly modeled but included by modifying the coefficient of elastic restitution [*Izard et al*., 2014; *Yang and Hunt*, 2006].

Lubrication forces are largest when particles nearly touch each other. A characteristic lubrication time scale, τ_{lub}, can be defined by evaluating F_{lub} at $\delta = 0$ and expressing how long it would take for the particle to travel over a characteristic distance when subjected to a normal stress of magnitude σ_N. *Coussot and Ancey* [1999] propose that this characteristic distance is the mean distance between the two centers of neighboring particles, which has the advantage of linking τ_{lub} to crystal volume fraction:

$$b = \frac{d}{2}\left(\frac{\phi_{\text{RCP}}}{\phi}\right)^{1/3} \tag{35}$$

where ϕ_{RCP} is the value of the random close packing. Recasting (35) as

$$\frac{3\pi\eta_f d^2\dot{\delta}}{2\delta_{\text{rough}}} = \frac{\pi d\sigma_n}{4} \tag{36}$$

and rearranging it yields

$$\dot{\delta} = \frac{\delta_{\text{rough}}\sigma_n}{12\eta_f} = \frac{b}{\tau_{\text{lub}}} \tag{37}$$

where

$$\tau_{\text{lub}} = \frac{12\eta_f b}{\delta_{\text{rough}}\sigma_n} \tag{38}$$

As discussed in section 4.3 below, the transition from a hydrodynamic state of fully lubricated contacts to a frictional, contact-dominated state by the breaking-down of lubricating melt films is associated with profound rheological changes, such as discontinuous shear thickening and jamming. This transition is expressed by a dimensionless number, s, which is proportional to $\tau_{\text{lub}}/\tau_{\text{macro}}$ [*Coussot and Ancey*, 1999]:

$$s = \frac{\eta_f b\dot{\gamma}}{\sigma_n\delta_{\text{rough}}} \tag{39}$$

The dimensionless number s given by (39) was called Leighton number by *Coussot and Ancey* [1999] but is currently more commonly referred to as the Sommerfeld number [*Fernandez et al*., 2013; *Stachowiak and Batchlor*, 2013]. At large values of s, the so-called hydrodynamic regime, a fluid layer separates the two particle surfaces and so the bulk coefficient of friction depends on the value of s, not just the dry value of the particle-particle friction coefficient. However, when $s \ll 1$, the system is in a contact frictional regime, the first normal stress difference is nonzero, and the bulk friction depends weakly on s and is described by the dry friction coefficient [*Clavaud et al*., 2017; *Fernandez et al*., 2013]. For geological applications we consider a roughness scale of δ_{rough} = 1 μm. In an environment where s is not spatially uniform jamming is initiated locally, and a hydrogranular media can manifest very heterogeneous irreversible behavior, a process perhaps common in crystal-rich magmas.

4.3. Jamming and Regimes of Dynamic Behavior

The jamming of granular materials is of wide interest and has been the subject of numerous reviews and ongoing investigation [*Andrea and Sidney*, 2010; *Banigan et al*., 2013; *Behringer*, 2015; *Grob et al*., 2014; *Siemens and van Hecke*, 2010; *van Hecke*, 2010]. A detailed exposition on the subject is beyond the scope of this work, so we will summarize a subset pertaining to frictional, viscous suspensions as that is of most relevance to magmatic processes; consideration of geological applications are given in section 5 below.

In the traditional scenario, jamming, also referred to as lock up, has been indexed to a critical particle volume fraction ϕ_{pc} where the viscosity diverges, and the material has finite bulk and shear moduli. However, volume fraction alone does not uniquely identify the spatial distribution of phases in that average volume, only the number. Relationships that attempt to relate porosity to coordination number, Z, have been proposed [*Field*, 1963; *Oda*, 1977; *Smith et al*., 1929], but this does not carry any information about which contacts are load bearing or their orientation. However, if the local void distribution is considered as a local fabric tensor as in equation (8), and then combined with other microstructural descriptions, it can add significant information [*Fu and Dafalias*, 2015; *Li and Li*, 2009].

For frictionless spheres jamming occurs through excluded volume effects and is generally understood to be the value of the random close packing, ϕ_{RCP}, which is approximately 0.64 in 3-D and 0.84 in 2-D [*Kamien and Liu*, 2007]. For frictional packings, the value of the packing depends on the particle friction coefficient and can go from the ϕ_{RCP} down to 0.54 in 3-D and 0.77 in 2-D which is often called random loose packing, ϕ_{RLP} [*Dong et al*., 2006; *Farrell et al*., 2010; *Onoda and Liniger*, 1990; *Song et al*., 2008]. This highlights the significance of particle friction in mediating the stress distribution and strength which is also expressed by changes in the coordination number (3). For example, the coordination number for frictionless particles at ϕ_{RCP} in 3-D is 5.96 and for 2-D it is 3.96 and for frictional spheres at ϕ_{RLP} is 3.88 in 3-D and 2.97 in 2-D (bidisperse) [*Silbert*, 2010]. The important observation is that an increase in friction yields jamming at a lower value of ϕ_{pc} at a corresponding lower value of the coordination number, Z. In our simulations shown in Figures 2 and 8, the coordination number is higher than that predicted by *Silbert* [2010]. This is because our initial packing was created by monodisperse particle settling in a vacuum, yielding an initial condition with a packing between ϕ_{RCP} and ϕ_{RLP} with some regions in a hexagonal coordination. Perfect 2-D hexagonal packing would produce an initial coordination of 6; the coordination number at the start of the simulation in Figure 2 was 4.8.

This jamming at lower values of ϕ in frictional systems is the result of the breakdown of lubrication and the onset of frictional contacts with the appearance of force chains as described in section 3.1 [*Fernandez et al*., 2013; *Ness and Sun*, 2016b; *Wyart and Cates*, 2014]. It is now understood that this process is fundamental to the rheology of hydrogranular flow and signals the onset of the so-called "boundary lubrication" frictional regime distinct from the "hydrodynamic" regime, where lubrication films are intact and particle friction plays almost no role [*Bi et al*., 2011; *Clavaud et al*., 2017; *Fernandez et al*., 2013; *Grob et al*., 2014; *Mari et al*., 2014]. A hydrogranular system in the hydrodynamic regime will jam at a value of $\phi = \phi_{\mathrm{RCP}}$, like that of frictionless systems.

The Sommerfeld number (39) provides the criteria for this transition between boundary and hydrodynamic states of lubrication and explains why there are two states of jamming possible in a hydrogranular systems: (1) In the hydrodynamic lubrication case, jamming occurs closer to a single value of ϕ and is not sensitive to values of particle friction coefficient, and (2) a so-called shear-jamming regime, associated with the onset of frictional contacts, the emergence of a force chain network, and a value of ϕ_{pc} that is not single-valued and depends explicitly on the value of the particle-particle friction coefficient. The emergence of frictional behavior is now understood as contributing to continuous (suspension viscosity is proportional to shear rate) and producing discontinuous (large discontinuous jumps in suspension viscosity as a function of shear rate) shear thickening as well [*Clavaud et al*., 2017; *Lin et al*., 2015; *Majumdar et al*., 2017; *Mari et al*., 2014; *Ness and Sun*, 2015, 2016a, 2016b; *Peters et al*., 2016; *Royer et al*., 2016; *Wyart and Cates*, 2014].

Hence, the presence of lubrication changes the traditional picture of the rheology in two ways. The first is that the progress to a rheological state and the value of ϕ_{pc} depends not only the shear rate but on the absolute value of the forces needed to initiate the boundary-lubrication regime. This is clearly expressed in (39), where normal forces compete with viscosity for control of the transition between the boundary and hydrodynamics states of lubrication and hence frictional control. Importantly, in the same system at the same time, the value of the lock up can be changing both locally and globally as a function of local crystal properties such as modal size distribution, orientation, and local stresses. There is no singular value of ϕ_{pc} that is globally applicable, as observed from diverse geological examples. The second implication is that phenomena like discontinuous shear thickening, often observed in hydrogranular systems, are not the same as a jammed state. It is a fragile condition, with intermittent flow [*Vitelli and van Hecke*, 2011], and depends

not only on the shear rate but also the value of the stress and the packing perhaps as observed in the experiments of *Picard et al*. [2013].

The inertial numbers can be employed to compose a constitutive model for hydrogranular media assuming a bulk friction law, widely known as the $\mu(I)$ rheology which accounts for shear thinning, thickening, and the onset of frictional behavior [*Boyer et al*., 2011; *Ness and Sun*, 2015, 2016a; *Trulsson et al*., 2012]. This rheology accommodates the importance of normal forces that arise from frictional particle contacts, a process that is not resolved in a suspension rheology (mixture theory) framing. If one assumes that the flow is homogeneous (affine),

$$\mu(I) = \mu_1 + 1.2K^{1/2} + .5K \tag{40}$$

where

$$K = I_{vg,P} + \alpha_I I_I^2 \tag{41}$$

and where the constant α_I is about 0.3 and where μ_1 can be taken as the bulk value of dry friction, commonly around 0.38. *Ness and Sun* [2016a] point out that this value is dependent on the value of the particle (local) friction and introduce a means of calculating that as a degree of freedom in the proposed rheology. Importantly, equation (40) does not diverge at a critical volume fraction like the traditional suspension rheology models do. However, this local rheology must be applied with caution close to the jamming transition where sustained frictional contacts produce both correlated motion and nonlocal conditions. *Staron et al*. [2010], *Gaume et al*. [2011], and *Zhang and Kamrin* [2017] suggest a correction for nonlocal behavior based on the notion of a field variable termed the "granular fluidity," which itself is defined in terms of a granular temperature.

Simplifications to (40) for applications to magmatic systems can be obtained by consideration of the scaled pressure,

$$\frac{I_{IP}}{I_{vP}} = \frac{d\sqrt{\alpha\rho_p P}}{\eta_f} \tag{42}$$

and a Stokes number based on the bulk shear rate, which is the time for momentum transport by viscous diffusion of the particle relative to the time for the particle to transit a neighboring particle [*Ness and Sun*, 2015; *Trulsson et al*., 2012],

$$St_B = \frac{I_{IP}^2}{I_{vP}} = \frac{\alpha\rho_p \dot{\gamma} d^2}{\eta_f} \tag{43}$$

where constants of order unity have been dropped for clarity. The transition from viscous to inertia dominated behavior is associated with a decrease in the dissipation from the interstitial fluid as St_B rises and has been observed to occur for values of the scaled pressure of around 5–15 and St_B of around unity [*Ness and Sun*, 2015, 2016a; *Trulsson et al*., 2012]. Note that their definition of St_B differs from ours in that they do not include the Darcy drag term, α. For typical crystal sizes and magma viscosities, St_B will be below unity and the inertia terms can be dropped for most applications except perhaps those obtained during exceptionally rapid magma transport and eruption. Thus, the viscous inertia number, either (30) or (31) is the appropriate dimensionless group to characterize the state of the system.

We illustrate this in Figure 10, where the simulation results from Figures 2e and 2f are contoured for the viscous number I_{vg} as given in equation (30). The white contour is a line dividing the portion of the system with a volume fraction of greater or less than 0.5. The red dashed line is the outline of the mixing bowl or the incipiently fluidized region. The color shading is the value of the viscous number from 10^{-3} to 1. The variable quantities in the viscous number are the shear rate and α which is calculated with (19), so variations in the viscous number directly reflect that. Note that for $\phi \leq 0.304$, α was set to 1/12, to avoid unrealistic values under dilute conditions. Recall that the viscous number is measure of the connectedness of the particle network with higher values indicating a diminished contiguity. This can been seen by comparing Figure 10 with Figure 2f, where the abundance of force chains is less in the regions with the higher values of the viscous

number. As the viscous number approaches unity the granular contact will be lost and the system will disassociate and become dilute. One implication is that the viscous number is a map of the mechanism of dissipation, from what might be called "viscogranular" at very low values to a mixed mode of viscous to transitional inertial with a Newtonian behavior (suspension) at higher values [see *Ness and Sun*, 2016a, Figure 1]. The Stokes number, St_B, based on equation (43), also reflects this transition, having a maximum value of around unity in the lower chimney of the conduit in Figure 10, where the viscous number is the highest, but generally being well below unity. Hence, Figure 10 provides a caution for the application of a simple rheological framework based on mixture theory to systems with spatially and temporally varying mixed modes of granular-to-viscous dissipation.

4.4. Nonspherical Particles

The discussion and simulations above are based on the assumption of spherical particles. This is a conceptual and computational convenience as there is hydrodynamic symmetry at low particle Reynolds number such that the particle drag and torque are insensitive to orientation. However, geological materials are not spherical [*Jerram et al*., 2003; *Picard et al*., 2013], and the extension of the framework described above to nonspherical conditions requires discussion in both the quasi-static modes of force transmission and the implicit reversibility imbedded in the applications of the inertia number in section 4.1 [*Coetzee*, 2017; *Zhong et al*., 2016].

The ways that a nonspherical particle differs from a spherical one is in the packing, coordination number, steric constraints, the changing of torque magnitude as a function of dominant force contact position along the surface, a nonuniform lubrication force (the watermelon seed effect), and the nonuniform hydrodynamic drag as a function of particle orientation in the fluid. In addition, nonspherical particles are likely to have an initial shape anisotropy distribution. Frictional elliptical particles deposited in viscous liquids can have lower values of ϕ_{RLP} compared to spheres and also have variable coordination numbers and a greater resistance to rotation which yields enhanced strength [*Baram and Lind*, 2012; *Baule and Makse*, 2014; *Borzsonyi and Stannarius*, 2013; *Delaney et al*., 2011; *Rothenburg and Bathurst*, 1993]. This reaffirms the point that porosity alone is not an adequate measure of system rheology. For example, *Mead and Cleary* [2015] demonstrated that modeling granular avalanches could only replicate natural examples if nonspherical particles were used. *Yamamoto and Matsuoka* [1997] and *Kawabata et al*. [2013] demonstrated how plate-like particles, a common shape of natural crystals, leads to distinct microstructures, shear banding, and kinematic features reminiscent of geological examples.

Nonspherical particles can also respond differently under dynamic conditions [*Moitra and Gonnermann*, 2015]. Consider a nonspherical particle displaced from a granular framework in shear. In section 4.1 the development of the local particle response time assumed an implicit hysteresis—that a particle could reconnect with the adjacent granular matrix by a simple reversal. But a nonspherical particle may undergo nonuniform hydrodynamic drag [*Dioguardi et al*., 2014; *Hölzer and Sommerfeld*, 2008; *Ouchene et al*., 2015] such that it can rotate, and re-establishing contact with the granular media may lead to a fragile connection. At large strains the shearing of nonspherical particles can lead to the irreversible formation of fluid melt pockets and so enhance unmixing and nonuniform particle distribution.

5. Applications to Geological Conditions

The principles of hydrogranular behavior may provide some guidance for the description and interpretation of natural processes. We illustrate this in Figure 11 where natural mush dynamics was assessed by considering the scenario of mush reactivation (see Figure 2) and that of thermal convection within the reservoir. The fields for both scenarios were calculated with typical parameters for felsic and mafic reservoirs, see the supporting information for details of the calculations. Within the framing in Figure 11, the "unlocking" of a crystal mush prior to mixing or eruption can be understood as a process that produces an increase in the viscous number and a decrease of the coordination number, whether initiated by a thermal event [*Burgisser and Bergantz*, 2011; *Huber et al*., 2011] or an overpressure from a new injection [*Bergantz et al*., 2015]. Importantly, unlocking can also occur simply by a small increase in the pore pressure as might occur during incipient vesiculation, allowing frictional contacts to relax and enter a state of lubrication. As long as some melt remains and maintains a connected network of pores, and if there is sufficient room for expansion, very small strain rates can mobilize viscous magmas producing unlocking. A process such as this may allow otherwise highly crystallized and cool systems to become rejuvenated [*Cooper and Kent*, 2014].

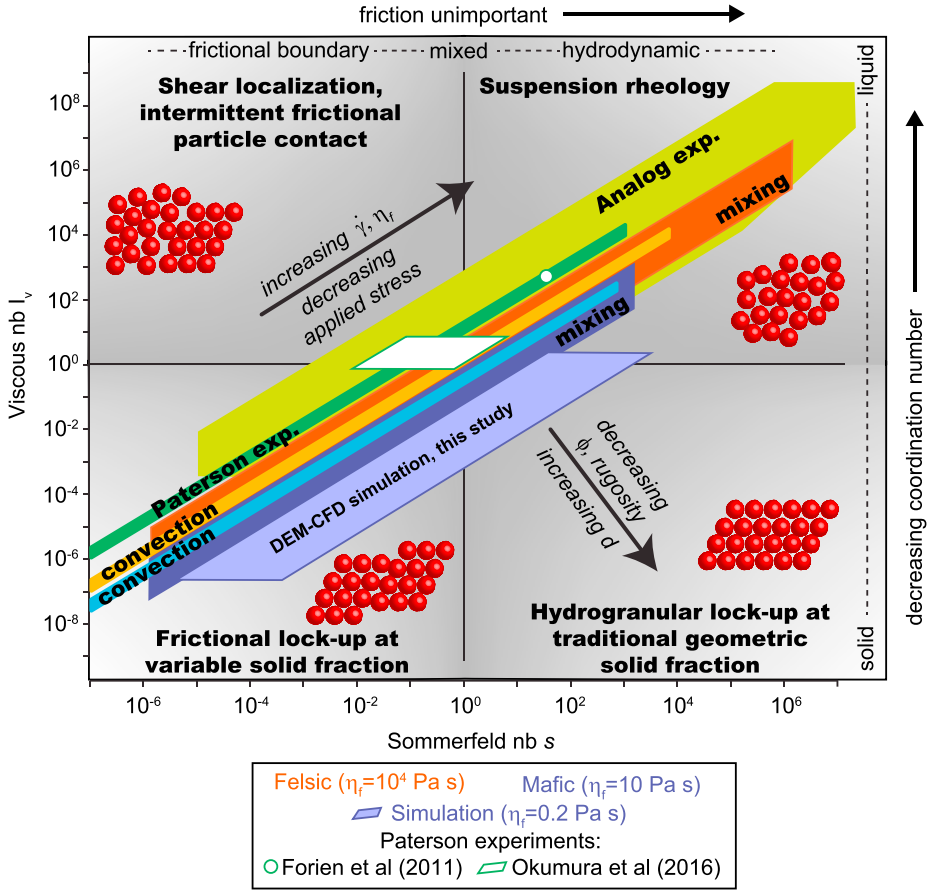

Figure 11. Natural mush dynamics fall mostly between the frictional hydrogranular regime, where particle-particle dynamics is dominated by frictional contacts and large coordination numbers and the classical suspension rheology, where coordination numbers are small and most of the suspension response is dominated by fluid tortuosity rather than interparticle contacts. Interestingly, the shear localization regime, where intermittent particle contact and strongly heterogeneous particle spatial distribution are expected, and the hydrodynamic regime, where lock-up is a material property and lubrication effects dominate particle-particle interactions, seem to be reached only under a restricted set of conditions in magmatic context. One important consequence of being in the frictional hydrogranular regime is that rheological lock-up does not occur at a crystal volume fraction depending only on geometrical parameters but is rather controlled by the dynamic state of the suspension. The arrows indicate the trends caused by changing only one variable at a time. The hydrogranular framework applies to dense systems, and we consider here that the dynamics of suspensions below 30 vol % crystals cannot be captured in this diagram. Values of α are like calculates with $C = 400$ to take particle rugosity into account. Experiments with analog materials and experiments done on real magmas in Paterson press apparatus cover well the natural ranges. Some experiments span different regime, while others are restricted to only one regime. As illustrated by two Paterson studies (white fields), it may be difficult to compare results from such pairs of experimental sets, despite having been carried out with the same apparatus. Conversely, experiments spanning several regimes may produce results challenging to interpret because of the complexity of their rheological response. See the supporting information for methods and values used to plot data fields. Calculation details in supporting information [*Androvandi et al.*, 2011; *Caricchi et al.*, 2008, 2014; *Castruccio et al.*, 2010; *Champallier et al.*, 2008; *Cimarelli et al.*, 2011; *Coetzee and Els*, 2009; *Dufek and Bergantz*, 2005; *Forien et al.*, 2011, 2015; *Girard and Stix*, 2009; *Grossmann and Lohse*, 2001; *Jellinek and DePaolo*, 2003; *Le Mével et al.*, 2016; *Okumura et al.*, 2016, 2015; *Parks et al.*, 2012; *Petrelli et al.*, 2016; *Pistone et al.*, 2012, 2015; *Rutherford*, 2008; *Walker et al.*, 1999].

It is beyond the scope of this work to review the numerous rheological models for (multiphase) magmatic systems; recent reviews include that of *Mader et al.* [2013] and *Picard et al.* [2013]. Setting the effects of crystal shape aside, the diversity of measured outcomes and nonunique critical melt fraction [*A Costa et al.*, 2009; *Moitra and Gonnermann*, 2015; *Petford*, 2009; *Philpotts et al.*, 1999; *Picard et al.*, 2013] may be attributable to microphysical feedback originating at crystal-crystal contacts. Hence, applying rheometric experiments to hydrogranular systems requires some caveats. Traditionally, the classic approach to suspension rheology assumes that the carrier phase, such as the melt, dominates the viscosity with the particles

only contributing to the dissipation and the emergence of normal stress differences close to lock-up. These rheological experiments are typically done under conditions of constant volume, subject to simple shear, producing a superficial Krieger-Dougherty-type suspension viscosity that diverges at the geometrical close packing. But it has been demonstrated that this experimental approach typically will not satisfy the requirements of spatial and temporal homogeneity for both flow and solid fractions [*Ancey et al*., 2013; *Ovarlez et al*., 2006; *Peters et al*., 2016], nor can they easily measure the friction or normal stress magnitudes to illuminate granular processes. Various approaches proposed to "correct" for nonsteady particle migration that arises from shear gradients and particle-particle interactions have been controversial [*Nott et al*., 2011] and depend specifically on the transport theory and application of interest with limited generality.

In addition, traditional rheology experiments may not represent the conditions of hydrogranular materials in a natural setting, where constant volume is not locally enforced and constant pressure (normal force) may be a more appropriate description of the ambient mechanical state. Under these conditions a hydrogranular mixture subject to shear is able to manifest normal stress differences and respond by dilation or compaction, and the viscosity does not become singular. Instead, a viscoplastic rheology is recovered where the shear to normal stress ratio approaches a constant value, as given in (40). Nor does a Krieger-Dougherty or other power law framing usually recover fragile states (as described in section 3.1) in natural materials at remarkably low particle volume fraction such as those reported by *Philpotts et al*. [1998], *Martin et al*. [2006], *Hoover et al*. [2001], and others. Nonetheless, as shown in Figure 11 some of the available analog experiments overlap the estimated parameter ranges of some magmatic processes; hence, it might be productive to revisit those experiments to further characterize the microscale hydrogranular particle interactions. As a result, rheometers may play a greater role as a "granular microscope" where detailed and highly resolved crystal-crystal-melt interactions can be characterized and cataloged as in *Moitra and Gonnermann* [2015]. Microcomputed tomography appears to be an especially promising approach to resolve emergent microscale behavior [*Dobson et al*., 2016].

A corollary to the rapid onset of frictional behavior as a function of the applied stress is the observation that hydrogranular materials can undergo progressive mechanical "solidification," upon impact [*Jerome et al*., 2016; *Peters et al*., 2016; *Waitukaitis and Jaeger*, 2012], a condition that occurs under extension as well [*Majumdar et al*., 2017]. Although pore pressure excursions associated with either dilation or compression upon impact (particle volume increase or decrease) mediate the onset of the boundary-lubrication frictional regime [*Jerome et al*., 2016], the occurrence of a jamming front that propagates away from the point of impact is well documented. This process may explain the observation that a crystal-bearing magma can temporarily manifest elastic-like behavior, for example, by supporting the injection by a dike with rather sharp boundaries, which as the dike progresses into the interior of the magma body where there is a deceasing crystal fraction, breaks up into a fountain-like feature. The idea is that as a dike enters a crystal-rich magma, the initial stress exerted on the crystal mush is sufficient to initiate a shear-jamming event that then provides support for the dike.

While our intended applications were implicitly to viscous hydrogranular systems, many of the same elements of description are applicable to granular volcanic processes that occur during eruption; the interested reader is directed to the work of *Estep and Dufek* [2012, 2013]. For example, in the case of dense granular pyroclastic flow, the viscosity of air plays a small role in the dissipation, the Sommerfeld number is vanishingly small, and the particles are in a state of friction. The appropriate dimensionless group would be the inertia number as given by (33), and a Bagnold scaling where the stress depends on the square of the shear rate [*Coussot and Ancey*, 1999].

The microscale kinematic description of a hydrogranular media as described in section 3 can provide some constraints on the scaling of analog and numerical experiments that attempt to probe their dynamics, e.g., [*Oppenheimer et al*., 2015; *Parmigiani et al*., 2016]. To establish verisimilitude with natural conditions involving both jammed and unjammed states, care must be taken initializing the particle framework so that microscale similarity is obtained. Currently, there is very little experimental guidance available to illuminate the appropriate choices for geological applications. Porosity alone is not an adequate measure of the mechanical state of a hydrogranular system, where even small differences in the method of construction can initialize the media with a history and anisotropic bias [*Daerr and Douady*, 1999; *Rondon et al*., 2011; *Vanel et al*., 1999]. Experiments on crystal-rich systems may require an uncertainty analysis for the initial condition prior to extending experimental results to natural applications. This may prove to be a challenge in rheology for multiphase magmas.

6. Concluding Remarks

The purpose of this work is to introduce and demonstrate kinematic and dynamic descriptions of hydrogranular (crystal-rich) systems in support of open questions regarding the behavior of magmas and migmatites. We demonstrated how crystal-rich systems can be described by contact and force tensors, and the anisotropy of these tensors is a direct reflection of the microstructure. We invoked the concept of force chains as a means of describing particle-particle interactions and emphasized that a breakdown in lubrication (melt films) can produce shear jamming that is not a function of shear rate but of applied normal stress, over a range of particle volume fractions. The implication of this is that within a magma body a jamming can occur well below the geometric value of lock-up, and the threshold can have many values simultaneously depending on local crystal shape, surface roughness, and melt viscosity. A corollary to this is that porosity alone is not an adequate state variable for rheological models. We introduced a viscous number that expressed the importance of melt viscosity relative to granular dissipation in controlling the tendency of the particle-rich system to disassociate, with a commensurate decrease in coordination number. We also introduced the Sommerfeld number, which is a measure of the state of lubrication at the particle-particle interface.

By combining the viscous number with the Sommerfeld number in a synoptic diagram, we identified four end-member behaviors. Invoking order of magnitude estimates for shear rate and normal stress, and combined with values typical of a range of geological settings, the likely field of possible outcomes was identified. We noted that while the available experiments on magma rheology appear to overlap significantly with the expected field of natural conditions, additional work is needed to characterize the results for microstructural analysis. We close by highlighting the need for more detailed assessments of the microgranular processes, with techniques taken from material science such as microcomputed tomography [*Dobson et al*., 2016] offering especially compelling opportunities for motivating more complete theory and integration with natural examples.

Acknowledgments
Financial support was provided by National Science Foundation grants EAR-1049884 and EAR-1447266 to G.W. B. and DGE-1256082 to J.M.S. A grant from Labex OSUG@2020 (ANR1O LABX56) partly supported A.B. Access to computational facilities was provided by grant TG-EAR140013 to G.W.B. from the NSF-funded XSEDE consortium. Dennis Geist and Valbone Memti are thanked for permission to use photographs in Figures 1a and 1c, respectively. Michael Walter and Luca Caricchi are thanked for professional and prompt editorial handling of the manuscript, and two anonymous reviewers for exceptionally helpful reviews. J. Sun, I.R. Peters, S.R. Paterson, and V. Memeti are acknowledged for helpful clarification. This work is dedicated to the 36th anniversary of the publication by B.D. Marsh, 1981, "On the crystallinity, probability of occurrence, and rheology of lava and magma," *Contributions to Mineralogy and Petrology*, v. 78. The open-source software, MFIX, used to create the simulation is available at https://mfix.netl.doe.gov/. The authors declare no competing financial interests.

References

Adam, J., S. Turner, and T. Rushmer (2016), The genesis of silicic arc magmas in shallow crustal cold zones, *Lithos*, *264*, 472–494, doi:10.1016/j.lithos.2016.07.036.

Ai, J., P. A. Langston, and H.-S. Yu (2014), Discrete element modelling of material non-coaxiality in simple shear flows, *Int. J. Numer. Anal. Met.*, *38*(6), 615–635, doi:10.1002/nag.2230.

Alizadeh, E., F. Bertrand, and J. Chaouki (2014), Comparison of DEM results and Lagrangian experimental data for the flow and mixing of granules in a rotating drum, *AIChE J.*, *60*(1), 60–75, doi:10.1002/aic.14259.

Allan, A. S. R., S. J. Barker, M.-A. Millet, D. J. Morgan, S. M. Rooyakkers, C. I. Schipper, and C. J. N. Wilson (2017), A cascade of magmatic events during the assembly and eruption of a super-sized magma body, *Contrib. Mineral. Petrol.*, *172*(7), 49, doi:10.1007/s00410-017-1367-8.

Ancey, C., N. Andreini, and G. Epely-Chauvin (2013), Granular suspension avalanches. I. Macro-viscous behavior, *Phys. Fluids*, *25*(3), 033301, doi:10.1063/1.4793719.

Andrea, J. L., and R. N. Sidney (2010), The jamming transition and the marginally jammed solid, *Annu. Rev. Cond. Matt. Phys.*, *1*(1), 347–369, doi:10.1146/annurev-conmatphys-070909-104045.

Andreotti, B., Y. Forterre, and O. Pouliquen (2013), *Granular Media : Between Fluid and Solid*, Cambridge Univ. Press, New York.

Androvandi, S., A. Davaille, A. Limare, A. Foucquier, and C. Marais (2011), At least three scales of convection in a mantle with strongly temperature-dependent viscosity, *Phys. Earth Planet. Inter.*, *188*(3), 132–141, doi:10.1016/j.pepi.2011.07.004.

Antony, S. J. (2007), Link between single-particle properties and macroscopic properties in particulate assemblies: Role of structures within structures, *Philos. Transact. A Math. Phys. Eng. Sci.*, *365*(1861), 2879–2891.

Bachmann, O., and G. W. Bergantz (2004), On the origin of crystal-poor rhyolites: Extracted from batholithic crystal mushes, *J. Petrol.*, *45*(8), 1565–1582.

Bachmann, O., and G. W. Bergantz (2008), The magma reservoirs that feed supereruptions, *Elements*, *4*, 17–21, doi:10.2113/GSELEMENTS.4.1.17.

Bachmann, O., M. A. Dungan, and P. W. Lipman (2002), The Fish Canyon magma body, San Juan volcanic field, Colorado: Rejuvenation and eruption of an upper crustal batholith, *J. Petrol.*, *43*, 1469–1503.

Bagnold, R. A. (1941), *The Physics of Blown Sand and Desert Dunes*, 265 pp., Methuen, London.

Bagnold, R. A. (1954), Experiments on a gravity-free dispersion of large solid spheres in a Newtonian fluid under shear, *Proc. R. Soc. London, Ser. A*, *225*(1160), 49–63, doi:10.1098/rspa.1954.0186.

Bak, P. (1996), *How Nature Works: The Science of Self-Organized Criticality*, Copernicus Press, New York.

Banigan, E. J., M. K. Illich, D. J. Stace-Naughton, and D. A. Egolf (2013), The chaotic dynamics of jamming, *Nat. Phys.*, *9*(5), 288–292, doi:10.1038/nphys2593.

Baram, R. M., and P. G. Lind (2012), Deposition of general ellipsoidal particles, *Phys. Rev. E*, *85*(4), 041301.

Barboni, M., P. Boehnke, A. K. Schmitt, T. M. Harrison, P. Shane, A.-S. Bouvier, and L. Baumgartner (2016), Warm storage for arc magmas, *Proc. Natl. Acad. Sci. U.S.A.*, *113*(49), 13,959–13,964, doi:10.1073/pnas.1616129113.

Bathurst, R. J., and L. Rothenburg (1990), Observations on stress-force-fabric relationships in idealized granular materials, *Mech. Mater.*, *9*(1), 65–80, doi:10.1016/0167-6636(90)90030-J.

Baule, A., and H. A. Makse (2014), Fundamental challenges in packing problems: From spherical to non-spherical particles, *Soft Matter*, *10*(25), 4423–4429, doi:10.1039/C3SM52783B.

Behringer, R. P. (2015), Jamming in granular materials, *Comptes Rendus Phys.*, *16*(1), 10–25, doi:10.1016/j.crhy.2015.02.001.

Behringer, R. P., D. Howell, L. Kondic, S. Tennakoon, and C. Veje (1999), Predictability and granular materials, *Physica D: Non. Phen.*, *133*(1–4), 1–17, doi:10.1016/S0167-2789(99)00094-9.
Bercovici, H., D. Geist, K. Harpp, M. Almeida, J. Mahr, R. Pimental, and Z. Cleary (2016), A little island with a big secret: Isla Rábida, Galápagos, Abstract V53C-3117 presented at 2016 Fall Meeting, AGU, San Francisco, Calif.
Bergantz, G. W., J. M. Schleicher, and A. Burgisser (2015), Open-system dynamics and mixing in magma mushes, *Nat. Geosci.*, *8*(10), 793–796, doi:10.1038/ngeo2534.
Bi, D., J. Zhang, B. Chakraborty, and R. P. Behringer (2011), Jamming by shear, *Nature*, *480*(7377), 355–358.
Biarez, J., and K. Wiendieck (1963), La comparison qualitative entre l'anisotropie mécanique et l'anisotropie de structure des milieux pulvérulents, *C. R. Acad. Sci.*, *256*, 1217–1220.
Borzsonyi, T., and R. Stannarius (2013), Granular materials composed of shape-anisotropic grains, *Soft Matter*, *9*(31), 7401–7418, doi:10.1039/C3SM50298H.
Bouzid, M., A. Izzet, M. Trulsson, E. Clément, P. Claudin, and B. Andreotti (2015a), Non-local rheology in dense granular flows, *Eur. Phys. J. E: Soft Matter Biol. Phys.*, *38*(11), 125, doi:10.1140/epje/i2015-15125-1.
Bouzid, M., M. Trulsson, P. Claudin, E. Clément, and B. Andreotti (2015b), Microrheology to probe non-local effects in dense granular flows, *Earth Planet. Lett. (Eur. Lett.)*, *109*(2), 24002.
Bouzid, M., M. Trulsson, P. Claudin, E. Clément, and B. Andreotti (2013), Nonlocal rheology of granular flows across yield conditions, *Phys. Rev. Lett.*, *111*(23), 238301.
Boyer, F., E. Guazzelli, and O. Pouliquen (2011), Unifying suspension and granular rheology, *Phys. Rev. Lett.*, *107*(18), 5, doi:10.1103/PhysRevLett.107.188301.
Brenner, H. (1961), The slow motion of a sphere through a viscous fluid towards a plane surface, *Chem. Eng. Sci.*, *16*(3), 242–251, doi:10.1016/0009-2509(61)80035-3.
Brewer, R. (1964), *Fabric and Mineral Analysis of Soils*, 470 pp., Wiley, New York.
Brown, M. (1994), The generation, segregation, ascent and emplacement of granite magma: The migmatite-to-crustally-derived granite connection in thickened orogens, *Earth Sci. Rev.*, *36*, 83–130.
Brown, M. (2004), The mechanism of melt extraction from lower continental crust of orogens, *Trans. R. Soc. Edinb. Earth Sci.*, *95*, 35–48.
Brown, M., A. Averkin, E. L. McLellan, and E. W. Sawyer (1995), Melt segregation in migmatites, *J. Geophys. Res.*, *100*, 15,655–15,679, doi:10.1029/95JB00517.
Burgisser, A., and G. W. Bergantz (2011), A rapid mechanism to remobilize and homogenize highly crystalline magma bodies, *Nature*, *471*(7337), 212–215, doi:10.1038/nature09799.
Burgisser, A., G. W. Bergantz, and R. E. Breidenthal (2005), Addressing complexity in laboratory experiments: The scaling of dilute multiphase flows in magmatic systems, *J. Volcanol. Geotherm. Res.*, *141*, 245–265.
Butler, S. L. (2012), Numerical models of shear-induced melt band formation with anisotropic matrix viscosity, *Phys. Earth Planet. Inter.*, *200–201*, 28–36, doi:10.1016/j.pepi.2012.03.011.
Campbell, C. S. (2006), Granular material flows—An overview, *Powder Technol.*, *162*, 208–229.
Caricchi, L., D. Giordano, L. Burlini, P. Ulmer, and C. Romano (2008), Rheological properties of magma from the 1538 eruption of Monte Nuovo (Phlegrean Fields, Italy): An experimental study, *Chem. Geol.*, *256*(3–4), 158–171, doi:10.1016/j.chemgeo.2008.06.035.
Caricchi, L., C. Annen, J. Blundy, G. Simpson, and V. Pinel (2014), Frequency and magnitude of volcanic eruptions controlled by magma injection and buoyancy, *Nat. Geosci.*, *7*(2), 126–130.
Casagrande, A., and N. Carrillo (1944), Shear failure of anistrophic materials, *J. Boston Soc. Civil Eng.*, *31*(2), 74–87.
Cassar, C., M. Nicolas, and O. Pouliquen (2005), Submarine granular flows down inclined planes, *Phys. Fluids*, *17*(10), 103301, doi:10.1063/1.2069864.
Castruccio, A., A. C. Rust, and R. S. J. Sparks (2010), Rheology and flow of crystal-bearing lavas: Insights from analogue gravity currents, *Earth Planet. Sci. Lett.*, *297*(3–4), 471–480, doi:10.1016/j.epsl.2010.06.051.
Cates, M. E., J. P. Wittmer, J. P. Bouchaud, and P. Claudin (1998), Jamming, force chains, and fragile matter, *Phys. Rev. Lett.*, *81*(9), 1841–1844.
Champallier, R., M. Bystricky, and L. Arbaret (2008), Experimental investigation of magma rheology at 300 MPa: From pure hydrous melt to 76 vol.% of crystals, *Earth Planet. Sci. Lett.*, *267*(3–4), 571–583, doi:10.1016/j.epsl.2007.11.065.
Charlier, B. L. A., O. Bachmann, J. P. Davidson, M. A. Dungan, and D. J. Morgan (2007), The upper crustal evolution of a large silicic magma body: Evidence from crystal-scale Rb-Sr isotopic heterogeneities in the Fish Canyon magmatic system, Colorado, *J. Petrol.*, *48*(10), 1875–1894, doi:10.1093/petrology/egm043.
Cimarelli, C., A. Costa, S. Mueller, and H. M. Mader (2011), Rheology of magmas with bimodal crystal size and shape distributions: Insights from analog experiments, *Geochem. Geophys. Geosyst.*, *12*, Q07024, doi:10.1029/2011GC003606.
Clavaud, C., A. Bérut, B. Metzger, and Y. Forterre (2017), Revealing the frictional transition in shear-thickening suspensions, *Proc. Natl. Acad. Sci. U.S.A.*, *114*(20), 5147–5152, doi:10.1073/pnas.1703926114.
Coetzee, C. J. (2017), Review: Calibration of the discrete element method, *Powder Technol.*, *310*, 104–142, doi:10.1016/j.powtec.2017.01.015.
Coetzee, C. J., and D. N. J. Els (2009), Calibration of discrete element parameters and the modelling of silo discharge and bucket filling, *Comput. Electron. Agric.*, *65*(2), 198–212, doi:10.1016/j.compag.2008.10.002.
Cole, D. M., and M. A. Hopkins (2016), The contact properties of naturally occurring geologic materials: Experimental observations, *Granul. Matter*, *18*(3), 62, doi:10.1007/s10035-016-0658-5.
Collins, W. J., R. A. Wiebe, B. Healy, and S. W. Richards (2006), Replenishment, crystal accumulation and floor aggradation in the megacrystic Kameruka Syite, Australia, *J. Petrol.*, *47*(11), 2073–2104.
Cooper, K. M., and A. J. R. Kent (2014), Rapid remobilization of magmatic crystals kept in cold storage, *Nature*, *506*(7489), 480–483, doi:10.1038/nature12991.
Costa, A., L. Caricchi, and N. Bagdassarov (2009), A model for the rheology of particle-bearing suspensions and partially molten rocks, *Geochem. Geophys. Geosyst.*, *10*, Q03010, doi:10.1029/2008GC002138.
Costa, F., L. A. Coogan, and S. Chakraborty (2010), The time scales of magma mixing and mingling involving primitive melts and melt–mush interaction at mid-ocean ridges, *Contrib. Mineral. Petrol.*, *159*, 371–387, doi:10.1007/s00410-009-0432-3.
Coulomb, C. A. (1776), Essai sur une application des règles de maximis & minimis à quelques problèmes de statique, relatifs à l'architecture, *Acad. Sci. Paris Mem. Math Phys.*, *7*, 343–382.
Coussot, P., and C. Ancey (1999), Rheophysical classification of concentrated suspensions and granular pastes, *Phys. Rev. E*, *59*(4), 4445–4457.
Crowe, C. T. (Ed.) (2006), *Multiphase Flow Handbook*, 1156 pp., CRC Press, Boca Raton, Fla.
Cundall, P. A., and O. D. L. Strack (1979), A discrete numerical model for granular assemblies, *Géotechnique*, *29*, 47–65.

Cundall, P. A., and O. D. L. Strack (1983), Modeling of microscopic mechanisms in granular material, in *Mechanics of Granular Materials: New Models and Constitutive Relations*, edited by J. T. Jenkins and M. Satake, pp. 137–149, Elsevier, Amsterdam.
Curray, J. R. (1956), The analysis of two-dimensional orientation data, *J. Geol.*, *64*(2), 117–131.
da Cruz, F., S. Emam, M. Prochnow, J.-N. Roux, and F. Chevoir (2005), Rheophysics of dense granular materials: Discrete simulation of plane shear flows, *Phys. Rev. E*, *72*(2), 021309.
Daerr, A., and S. Douady (1999), Sensitivity of granular surface flows to preparation, *Earth Planet. Lett. (Eur. Lett.)*, *47*(3), 324.
Dantu, P. (1957), Contribution à l'Étude Mécanique et Géométrique des Milieux Pulvérulents, paper presented at Proc. Of the 4th International Conf. On Soil Mech. and Foundation Eng., Butterworths Sci. Publ.
Davidson, J. P., F. J. Tepley III, Z. Palazc, and S. Meffan-Main (2001), Magma recharge, contamination and residence times revealed by in situ laser ablation isotopic analysis of feldspar in volcanic rocks, *Earth Planet. Sci. Lett.*, *184*, 427–442.
de Jong, G. D. J., and A. Verruijt (1969), Étude photo-Élastique d'un empilement de disques, *Cahiers du Groupe Francis de Rhéologie*, *2*(1), 73–86, doi:10.1007/978-1-4020-3629-3_15.
de Silva, S. L., and P. M. Gregg (2014), Thermomechanical feedbacks in magmatic systems: Implications for growth, longevity, and evolution of large caldera-forming magma reservoirs and their supereruptions, *J. Volcanol. Geotherm. Res.*, *282*, 77–91, doi:10.1016/j.jvolgeores.2014.06.001.
Delaney, G. W., J. E. Hilton, and P. W. Cleary (2011), Defining random loose packing for nonspherical grains, *Phys. Rev. E*, *83*(5), 051305.
Delannay, R., A. Valance, A. Mangeney, O. Roche, and P. Richard (2017), Granular and particle-laden flows: From laboratory experiments to field observations, *J. Phys. D: Appl. Phys.*, *50*(5), 053001.
Dioguardi, F., P. Dellino, and D. Mele (2014), Integration of a new shape-dependent particle–fluid drag coefficient law in the multiphase Eulerian–Lagrangian code MFIX-DEM, *Powder Technol.*, *260*, 68–77, doi:10.1016/j.powtec.2014.03.071.
Dobson, K. J., S. B. Coban, S. A. McDonald, J. N. Walsh, R. C. Atwood, and P. J. Withers (2016), 4-D imaging of sub-second dynamics in pore-scale processes using real-time synchrotron X-ray tomography, *Solid Earth*, *7*(4), 1059–1073, doi:10.5194/se-7-1059-2016.
Dong, K. J., R. Y. Yang, R. P. Zou, and A. B. Yu (2006), Role of interparticle forces in the formation of random loose packing, *Phys. Rev. Lett.*, *96*(14), 145505.
Dufek, J., and G. W. Bergantz (2005), Lower crustal magma genesis and preservation: A stochastic framework for the evaluation of basalt-crust interaction, *J. Petrol.*, *46*(11), 2167–2196.
Duran, J. (2000), *Sands, Powders, and Grains: An Introduction to the Physics of Granular Materials*, 214 pp., Springer, New York.
Estep, J., and J. Dufek (2012), Substrate effects from force chain dynamics in dense granular flows, *J. Geophys. Res.*, *117*, F01028, doi:10.1029/2011JF002125.
Estep, J., and J. Dufek (2013), Discrete element simulations of bed force anomalies due to force chains in dense granular flows, *J. Volcanol. Geotherm. Res.*, *254*, 108–117, doi:10.1016/j.jvolgeores.2012.12.023.
Farrell, G. R., K. M. Martini, and N. Menon (2010), Loose packings of frictional spheres, *Soft Matter*, *6*(13), 2925–2930, doi:10.1039/C0SM00038H.
Fernandez, N., R. Mani, D. Rinaldi, D. Kadau, M. Mosquet, H. Lombois-Burger, J. Cayer-Barrioz, H. J. Herrmann, N. D. Spencer, and L. Isa (2013), Microscopic mechanism for shear thickening of non-Brownian suspensions, *Phys. Rev. Lett.*, *111*(10), 108301.
Field, W. G. (1963), Towards a statistical definition of granular mass, in *Fourth Australian and New Zealand Conference on Soil Mechanics and Foundation Engineering*, pp. 143–148, Inst. of Eng., Sydney, Australia.
Forien, M., L. Arbaret, A. Burgisser, and R. Champallier (2011), Experimental constrains on shear-induced crystal breakage in magmas, *J. Geophys. Res.*, *116*, B08217, doi:10.1029/2010JB008026.
Forien, M., J. Tremblay, S.-J. Barnes, A. Burgisser, and P. Pagé (2015), The role of viscous particle segregation in forming chromite layers from slumped crystal slurries: Insights from analogue experiments, *J. Petrol.*, *56*(12), 2425–2444, doi:10.1093/petrology/egv060.
Forterre, Y., and O. Pouliquen (2008), Flows of dense granular media, in *Annual Review Fluid Mechanics*, pp. 1–24, Annual Reviews, Palo Alto, doi:10.1146/annurev.fluid.40.111406.102142.
Franklin, S. V., and M. D. Shattuck (Eds.) (2015), *Handbook of Granular Materials*, 506 pp., CRC Press, Boca Raton, Fla.
Friedman, G. M. (1965), Terminology of crystallization textures and fabrics in sedimentary rocks, *J. Sediment. Res.*, *35*(3), 643–655, doi:10.1306/74d7131b-2b21-11d7-8648000102c1865d.
Fu, P., and Y. F. Dafalias (2015), Relationship between void- and contact normal-based fabric tensors for 2D idealized granular materials, *Int. J. Solids Struct.*, *63*, 68–81, doi:10.1016/j.ijsolstr.2015.02.041.
Garg, R., J. Galvin, T. Li, and S. Pannala (2012a), Documentation of open-source MFIX-DEM software for gas-solids flows. [Available at https://mfix.netl.doe.gov/documentation/dem_doc_2012-1.pdf.]
Garg, R., J. Galvin, T. Li, and S. Pannala (2012b), Open-source MFIX-DEM software for gas–solids flows: Part I—Verification studies, *Powder Technol.*, *220*, 122–137, doi:10.1016/j.powtec.2011.09.019.
Gaume, J., G. Chambon, and M. Naaim (2011), Quasistatic to inertial transition in granular materials and the role of fluctuations, *Phys. Rev. E*, *84*(5), 051304.
Gipson, M. (1965), Application of the electron microscope to the study of particle orientation and fissility in shale, *J. Sediment. Res.*, *35*(2), 408–414, doi:10.1306/74d7128f-2b21-11d7-8648000102c1865d.
Girard, G., and J. Stix (2009), Buoyant replenishment in silicic magma reservoirs: Experimental approach and implications for magma dynamics, crystal mush remobilization, and eruption, *J. Geophys. Res.*, *114*, B08203, doi:10.1029/2008JB005791.
Grob, M., C. Heussinger, and A. Zippelius (2014), Jamming of frictional particles: A nonequilibrium first-order phase transition, *Phys. Rev. E*, *89*(5), 050201.
Grossmann, S., and D. Lohse (2001), Thermal convection for large Prandtl numbers, *Phys. Rev. Lett.*, *86*(15), 3316–3319.
Guo, P. (2012), Critical length of force chains and shear band thickness in dense granular materials, *Acta Geotech.*, *7*, 41–55, doi:10.1007/sl1440-011-0154-3.
Gutiérrez, F., I. Payacán, S. E. Gelman, O. Bachmann, and M. A. Parada (2013), Late-stage magma flow in a shallow felsic reservoir: Merging the anisotropy of magnetic susceptibility record with numerical simulations in La Gloria Pluton, central Chile, *J. Geophys. Res. Solid Earth*, *118*, 1984–1998, doi:10.1002/jgrb.50164.
Haff, P. K. (1983), Grain flow as a fluid-mechanical phenomenon, *J. Fluid Mech.*, *134*, 401–430, doi:10.1017/S0022112083003419.
Hertz, H. (1882), Ueber die Berührung fester elastischer Körper, in *Journal für die reine und angewandte Mathematik*, pp. 156–171, De Gruyter, Berlin, doi:10.1515/crll.1882.92.156.
Hildreth, W. (2004), Volcanological perspectives on Long Valley, Mammoth Mountain, and Mono Craters: Several contiguous but discrete systems, *J. Volcanol. Geotherm. Res.*, *136*, 169–198.
Hill, R. (1950), *The Mathematical Theory of Plasticity*, Oxford Univ. Press, Oxford.

Holness, M. B., A. T. Anderson, V. M. Martin, J. Maclennan, E. Passmore, and K. Schwindinger (2007), Textures in partially solidified crystalline nodules: A window into the pore structure of slowly cooled mafic intrusions, *J. Petrol.*, *48*(7), 1243–1264, doi:10.1093/petrology/egm016.

Hölzer, A., and M. Sommerfeld (2008), New simple correlation formula for the drag coefficient of non-spherical particles, *Powder Technol.*, *184*(3), 361–365, doi:10.1016/j.powtec.2007.08.021.

Hoover, S. R., K. V. Cashman, and M. Manga (2001), The yield strength of subliquidus basalts—Experimental results, *J. Volcanol. Geotherm. Res.*, *107*(1–3), 1–18, doi:10.1016/S0377-0273(00)00317-6.

Huber, C., O. Bachmann, and J. Dufek (2011), Thermo-mechanical reactivation of locked crystal mushes: Melting-induced internal fracturing and assimilation processes in magmas, *Earth Planet. Sci. Lett.*, *304*(3–4), 443–454, doi:10.1016/j.epsl.2011.02.022.

Hurley, R. C., S. A. Hall, J. E. Andrade, and J. Wright (2016), Quantifying interparticle forces and heterogeneity in 3D granular materials, *Phys. Rev. Lett.*, *117*(9), 098005.

Iverson, R. M. (1997), The physics of debris flows, *Rev. Geophys.*, *35*, 245–296, doi:10.1029/97RG00426.

Iverson, R. M., M. E. Reid, N. R. Iverson, R. G. LaHusen, M. Logan, J. E. Mann, and D. L. Brien (2000), Acute sensitivity of landslide rates to initial soil porosity, *Science*, *290*(5491), 513–516, doi:10.1126/science.290.5491.513.

Izard, E., T. Bonometti, and L. Lacaze (2014), Modelling the dynamics of a sphere approaching and bouncing on a wall in a viscous fluid, *J. Fluid Mech.*, *747*, 422–446, doi:10.1017/jfm.2014.145.

Jellinek, A. M., and D. J. DePaolo (2003), A model for the origin of large silicic magma chambers: Precursors of caldera-forming eruptions, *Bull. Volcanol.*, *65*(5), 363–381, doi:10.1007/s00445-003-0277-y.

Jerome, J. J. S., N. Vandenberghe, and Y. Forterre (2016), Unifying impacts in Granul. Matter from quicksand to cornstarch, *Phys. Rev. Lett.*, *117*(9), 098003, doi:10.1103/PhysRevLett.117.098003.

Jerram, D. A., M. J. Cheadle, and A. R. Philpotts (2003), Quantifying the building blocks of igneous rocks: Are clustered crystal frameworks the foundation?, *J. Petrol.*, *44*, 2033–2051.

Jiang, M., J. Sima, L. Li, C. Zhou, and L. Cui (2017), Investigation of influence of particle characteristics on the non-coaxiality of anisotropic granular materials using DEM, *Int. J. Numer. Anal. Met.*, *41*(2), 198–222, doi:10.1002/nag.2551.

Kaiser, J. F., S. L. de Silva, A. K. Schmitt, R. Economos, and M. Sunagua (2017), Million-year melt–presence in monotonous intermediate magma for a volcanic–plutonic assemblage in the Central Andes: Contrasting histories of crystal-rich and crystal-poor super-sized silicic magmas, *Earth Planet. Sci. Lett.*, *457*, 73–86, doi:10.1016/j.epsl.2016.09.048.

Kamien, R. D., and A. J. Liu (2007), Why is random close packing reproducible?, *Phys. Rev. Lett.*, *99*(15), 155501.

Kanai, H., R. C. Navarrete, C. W. Macosko, and L. E. Scriven (1992), Fragile networks and rheology of concentrated suspensions, *Rheol. Acta*, *31*(4), 333–344, doi:10.1007/bf00418330.

Kanatani, K. (1984), Distribution of directional data and fabric tensors, *Int. J. Eng. Sci.*, *22*(2), 149–164, doi:10.1016/0020-7225(84)90090-9.

Katz, R. F., M. Spiegelman, and B. Holtzman (2006), The dynamics of melt and shear localization in partially molten aggregates, *Nature*, *442*(7103), 676–679.

Kawabata, H., D. Nishiura, H. Sakaguchi, and Y. Tatsumi (2013), Self-organized domain microstructures in a plate-like particle suspension subjected to rapid simple shear, *Rheol. Acta*, *52*(1), 1–21, doi:10.1007/s00397-012-0657-3.

Kim, S., and S. J. Karrila (1991), *Microhydrodynamics Principles and Selected Applications*, 507 pp., Butterworth-Heinemann, Boston, Mass.

Klemetti, E. W., and M. A. Clynne (2014), Localized rejuvenation of a crystal mush recorded in zircon temporal and compositional variation at the Lassen Volcanic Center, Northern California, *PLoS One*, *9*(12), e113157, doi:10.1371/journal.pone.0113157.

Kruyt, N. P., and L. Rothenburg (2016), A micromechanical study of dilatancy of granular materials, *J. Mech. Phys. Solids*, *95*, 411–427, doi:10.1016/j.jmps.2016.01.019.

Laird, M. G. (1970), Vertical sheet structures: A new indicator of sedimentary fabric, *J. Sediment. Res.*, *40*(1), 428–434, doi:10.1306/74d71f69-2b21-11d7-8648000102c1865d.

Le Mével, H., P. M. Gregg, and K. L. Feigl (2016), Magma injection into a long-lived reservoir to explain geodetically measured uplift: Application to the 2007–2014 unrest episode at Laguna del Maule volcanic field, Chile, *J. Geophys. Res. Solid Earth*, *121*, 6092–6108, doi:10.1002/2016JB013066.

Li, T., and C. Guenther (2012), MFIX-DEM simulations of change of volumetric flow in fluidized beds due to chemical reactions, *Powder Technol.*, *220*, 70–78, doi:10.1016/j.powtec.2011.09.025.

Li, T., R. Garg, J. Galvin, and S. Pannala (2012), Open-source MFIX-DEM software for gas-solids flows: Part II—Validation studies, *Powder Technol.*, *220*, 138–150, doi:10.1016/j.powtec.2011.09.020.

Li, X., and X. S. Li (2009), Micro-macro quantification of the internal structure of granular materials, *J. Eng. Mech.*, *135*(7), 641–656, doi:10.1061/(ASCE)0733-9399(2009)135:7(641).

Lin, G., F. Amelung, Y. Lavallée, and P. G. Okubo (2014), Seismic evidence for a crustal magma reservoir beneath the upper east rift zone of Kilauea volcano, Hawaii, *Geology*, *42*(3), 187–190, doi:10.1130/g35001.1.

Lin, N. Y. C., B. M. Guy, M. Hermes, C. Ness, J. Sun, W. C. K. Poon, and I. Cohen (2015), Hydrodynamic and contact contributions to continuous shear thickening in colloidal cuspensions, *Phys. Rev. Lett.*, *115*(22), 228304, doi:10.1103/PhysRevLett.115.228304.

Lindsay, J. M., A. K. Schmitt, R. B. Trumbull, S. L. De Silva, W. Siebel, and R. Emmermann (2001), Magmatic evolution of the La Pacana caldera system, central Andes, Chile: Compositional variation of two cogenetic large-volume felsic ignimbrites, *J. Petrol.*, *42*(3), 459–486.

Madadi, M., O. Tsoungui, M. Lätzel, and S. Luding (2004), On the fabric tensor of polydisperse granular materials in 2D, *Int. J. Solids Struct.*, *41*(9–10), 2563–2580, doi:10.1016/j.ijsolstr.2003.12.005.

Mader, H. M., E. W. Llewellin, and S. P. Mueller (2013), The rheology of two-phase magmas: A review and analysis, *J. Volcanol. Geotherm. Res.*, *257*, 135–158, doi:10.1016/j.jvolgeores.2013.02.014.

Majmudar, T. S., and R. P. Behringer (2005), Contact force measurements and stress-induced anisotropy in granular materials, *Nature*, *435*(1079), 1079–1082.

Majumdar, S., I. R. Peters, E. Han, and H. M. Jaeger (2017), Dynamic shear jamming in dense granular suspensions under extension, *Phys. Rev. E*, *95*(1), 012603.

Mansard, V., and A. Colin (2012), Local and non local rheology of concentrated particles, *Soft Matter*, *8*(15), 4025–4043, doi:10.1039/C2SM25306B.

Mari, R., R. Seto, J. F. Morris, and M. M. Denn (2014), Shear thickening, frictionless and frictional rheologies in non-Brownian suspensions, *J. Rheol.*, *58*(6), 1693–1724, doi:10.1122/1.4890747.

Marsh, B. D. (1981), On the crystallinity, probability of occurrence, and rheology of lava and magma, *Contrib. Mineral. Petrol.*, *78*, 85–98.

Martin, V. M., D. M. Pyle, and M. B. Holness (2006), The role of crystal frameworks in the preservation of enclaves during magma mixing, *Earth Planet. Sci. Lett.*, *248*(3–4), 787–799, doi:10.1016/j.epsl.2006.06.030.

Marzougui, D., B. Chareyre, and J. Chauchat (2015), Microscopic origins of shear stress in dense fluid–grain mixtures, *Granul. Matter*, *17*(3), 297–309, doi:10.1007/s10035-015-0560-6.
McBirney, A. R., A. E. Boudreau, and B. D. Marsh (2009), Comments on: 'Textural maturity of cumulates: A record of chamber filling, liquidus assemblage, cooling rate and large-scale convection in mafic layered intrusions' and 'A textural record of solidification and cooling in the Skaergaard intrusion, East Greenland', *J. Petrol.*, *50*(1), 93–95, doi:10.1093/petrology/egn073.
Mead, S. R., and P. W. Cleary (2015), Validation of DEM prediction for granular avalanches on irregular terrain, *J. Geophys. Res. Earth Surf.*, *120*, 1724–1742, doi:10.1002/2014JF003331.
Meier, S. W., R. M. Lueptow, and J. M. Ottino (2007), A dynamical systems approach to mixing and segregation of granular materials in tumblers, *Adv. Phys.*, *56*(5), 757–827, doi:10.1080/00018730701611677.
MiDi, G. (2004), On dense granular flows, *Eur. Phys. J. E: Soft Matter Biol. Phys.*, *14*(4), 341–365, doi:10.1140/epje/i2003-10153-0.
Modaressi, A., S. Boufellouh, and P. Evesque (1999), Modeling of stress distribution in granular piles: Comparison with centrifuge experiments, *Chaos*, *9*(3), 523–543, doi:10.1063/1.166427.
Moitra, P., and H. M. Gonnermann (2015), Effects of crystal shape- and size-modality on magma rheology, *Geochem. Geophys. Geosyst.*, *16*, 1–26, doi:10.1002/2014GC005554.
Mutabaruka, P., J.-Y. Delenne, K. Soga, and F. Radjai (2014), Initiation of immersed granular avalanches, *Phys. Rev. E*, *89*(5), 052203.
Muthuswamy, M., and A. Tordesillas (2006), How do interparticle contact friction, packing density and degree of polydispersity affect force propagation in particulate assemblies?, *J. Stat. Mech.: Theory Experience*, *2006*(09), P09003.
Nakamura, H., and S. Watano (2007), Numerical modeling of particle fluidization behavior in a rotating fluidized bed, *Powder Technol.*, *171*(2), 106–117, doi:10.1016/j.powtec.2006.08.021.
Ness, C., and J. Sun (2015), Flow regime transitions in dense non-Brownian suspensions: Rheology, microstructural characterization, and constitutive modeling, *Phys. Rev. E*, *91*(1), 012201.
Ness, C., and J. Sun (2016a), Shear thickening regimes of dense non-Brownian suspensions, *Soft Matter*, doi:10.1039/C5SM02326B.
Ness, C., and J. Sun (2016b), Two-scale evolution during shear reversal in dense suspensions, *Phys. Rev. E*, *93*(1), 012604.
Ness, C., Z. Xing, and E. Eiser (2017), Oscillatory rheology of dense, athermal suspensions of nearly hard spheres below the jamming point, *Soft Matter*, *13*(19), 3664–3674, doi:10.1039/C7SM00039A.
Nicolas, A. (1992), Kinematics in magmatic rocks with special reference to gabbros, *J. Petrol.*, *33*, 891–915.
Nott, P. R., E. Guazzelli, and O. Pouliquen (2011), The suspension balance model revisited, *Phys. Fluids*, *23*(4), 043304, doi:10.1063/1.3570921.
Oda, M. (1972), The mechanism of frabic changes during compressional deformation of sand, *Soils Found.*, *12*(2), 1–18, doi:10.3208/sandf1972.12.1.
Oda, M. (1977), Co-ordination number and its relation to shear strength of granular material, *Soils Found.*, *17*(2), 29–42, doi:10.3208/sandf1972.17.2_29.
Oda, M., and J. Konishi (1974), Microscopic deformation mechanism of granular material in simple shear, *Soils Found.*, *14*(4), 25–38, doi:10.3208/sandf1972.14.4_25.
Oda, M., and K. Iwashita (Eds.) (1999), *Mechanics of Granular Materials: An Introduction*, 383 pp., A.A. Balkema, Rotterdam.
Oda, M., S. Nemat-Nasser, and J. Konishi (1985), Stress-induced anistrophy in granular masses, *Soils Found.*, *25*(3), 85–97, doi:10.3208/sandf1972.25.3_85.
Okumura, S., K. Uesugi, M. Nakamura, and O. Sasaki (2015), Rheological transitions in high-temperature volcanic fault zones, *J. Geophys. Res. Solid Earth*, *120*, 2974–2987, doi:10.1002/2014JB011532.
Okumura, S., A. R. L. Kushnir, C. Martel, R. Champallier, Q. Thibault, and S. Takeuchi (2016), Rheology of crystal-bearing natural magmas: Torsional deformation experiments at 800 °C and 100 MPa, *J. Volcanol. Geotherm. Res.*, *328*, 237–246, doi:10.1016/j.jvolgeores.2016.11.009.
Onoda, G. Y., and E. G. Liniger (1990), Random loose packings of uniform spheres and the dilatancy onset, *Phys. Rev. Lett.*, *64*(22), 2727–2730.
Oppenheimer, J., A. Rust, K. Cashman, and B. Sandnes (2015), Gas migration regimes and outgassing in particle-rich suspensions, *Front. Phys.*, *3*(60), doi:10.3389/fphy.2015.00060.
Ouchene, R., M. Khalij, A. Tanière, and B. Arcen (2015), Drag, lift and torque coefficients for ellipsoidal particles: From low to moderate particle Reynolds numbers, *Comput. Fluids*, *113*, 53–64, doi:10.1016/j.compfluid.2014.12.005.
Ovarlez, G., F. Bertrand, and S. Rodts (2006), Local determination of the constitutive law of a dense suspension of noncolloidal particles through magnetic resonance imaging, *J. Rheol.*, *50*(3), 259–292, doi:10.1122/1.2188528.
Pailha, M., M. Nicolas, and O. Pouliquen (2008), Initiation of underwater granular avalanches: Influence of the initial volume fraction, *Phys. Fluids*, *20*(11), 111701, doi:10.1063/1.3013896.
Parks, M. M., et al. (2012), Evolution of Santorini Volcano dominated by episodic and rapid fluxes of melt from depth, *Nat. Geosci.*, *5*(10), 749–754.
Parmigiani, A., S. Faroughi, C. Huber, O. Bachmann, and Y. Su (2016), Bubble accumulation and its role in the evolution of magma reservoirs in the upper crust, *Nature*, *532*(7600), 492–495, doi:10.1038/nature17401.
Paterson, S. R. (2009), Magmatic tubes, pipes, troughs, diapirs, and plumes: Late-stage convective instabilities resulting in compositional diversity and permeable networks in crystal-rich magmas of the Tuolumne batholith, Sierra Nevada, California, *Geosphere*, *5*(6), 496–527, doi:10.1130/ges00214.1.
Paterson, S. R., J. Žák, and V. Janoušek (2008), Growth of complex sheeted zones during recycling of older magmatic units into younger: Sawmill Canyon area, Tuolumne batholith, Sierra Nevada, California, *J. Volcanol. Geotherm. Res.*, *177*(2), 457–484, doi:10.1016/j.jvolgeores.2008.06.024.
Paterson, S. R., V. Memeti, R. Mundil, and J. Žák (2016), Repeated, multiscale, magmatic erosion and recycling in an upper-crustal pluton: Implications for magma chamber dynamics and magma volume estimates, *Am. Mineral.*, *101*(10), 2176–2198, doi:10.2138/am-2016-5576.
Paulick, M., M. Morgeneyer, and A. Kwade (2015), Review on the influence of elastic particle properties on DEM simulation results, *Powder Technol.*, *283*, 66–76, doi:10.1016/j.powtec.2015.03.040.
Peng, Z., E. Doroodchi, C. Luo, and B. Moghtaderi (2014), Influence of void fraction calculation on fidelity of CFD-DEM simulation of gas-solid bubbling fluidized beds, *AIChE J.*, *60*(6), 2000–2018, doi:10.1002/aic.14421.
Peters, I. R., S. Majumdar, and H. M. Jaeger (2016), Direct observation of dynamic shear jamming in dense suspensions, *Nature*, *532*(7598), 214–217, doi:10.1038/nature17167.
Peters, J. F., M. Muthuswamy, J. Wibowo, and A. Tordesillas (2005), Characterization of force chains in granular material, *Phys. Rev. E*, *72*(4), 041307.
Petford, N. (2009), Which effective viscosity?, *Min. Mag.*, *73*(2), 167–191, doi:10.1180/minmag.2009.073.2.167.
Petrelli, M., K. El Omari, Y. Le Guer, and D. Perugini (2016), Effects of chaotic advection on the timescales of cooling and crystallization of magma bodies at mid crustal levels, *Geochem. Geophys. Geosyst.*, *17*, 425–441, doi:10.1002/2015GC006109.

Philpotts, A. R., J. Shi, and C. Brustman (1998), Role of plagioclase crystal chains in the differentiation of partly crystallized basaltic magma, *Nature*, *395*, 343–346.
Philpotts, A. R., C. M. Brustman, J. Shi, W. D. Carlson, and C. Denison (1999), Plagioclase-chain networks in slowly cooled basaltic magma, *Am. Mineral.*, *84*, 1819–1820.
Picard, D., L. Arbaret, M. Pichavant, R. Champallier, and P. Launeau (2013), The rheological transition in plagioclase-bearing magmas, *J. Geophys. Res. Solid Earth*, *118*, 1363–1377, doi:10.1002/jgrb.50091.
Pistone, M., L. Caricchi, P. Ulmer, L. Burlini, P. Ardia, E. Reusser, F. Marone, and L. Arbaret (2012), Deformation experiments of bubble- and crystal-bearing magmas: Rheological and microstructural analysis, *J. Geophys. Res.*, *117*, B05208, doi:10.1029/2011JB008986.
Pistone, M., B. Cordonnier, L. Caricchi, P. Ulmer, and F. Marone (2015), The viscous to brittle transition in crystal- and bubble-bearing magmas, *Front. Earth Sci.*, *3*(71), doi:10.3389/feart.2015.00071.
Pritchard, M. E., and P. M. Gregg (2016), Geophysical evidence for silicic crustal melt in the continents: Where, what kind, and how much?, *Elements*, *12*(2), 121–127, doi:10.2113/gselements.12.2.121.
Radjai, F., M. L. Jean, J. Moreau, and S. Roux (1996), Force distributions in dense two-dimensional granular systems, *Phys. Rev. Lett.*, *77*(2), 274–277.
Radjai, F., D. E. Wolf, M. Jean, and J. Moreau (1998), Bimodal character of stress transmission in granular packings, *Phys. Rev. Lett.*, *80*(1), 61–64.
Radjai, F., J.-Y. Delenne, E. Azéma, and S. Roux (2012), Fabric evolution and accessible geometrical states in granular materials, *Granul. Matter*, *14*(2), 259–264, doi:10.1007/s10035-012-0321-8.
Reynolds, O. (1885), *LVII. On the Dilatancy of Media Composed of Rigid Particles in Contact. With Experimental Illustrations*, *Phil. Magazine Series 5*, 20(127), 469–481, doi:10.1080/14786448508627791.
Rhodes, J. M. (1995), The 1852 and 1868 Mauna Loa picrite eruptions: Clues to parental magma compositions and the magmatic plumbing system, in *Mauna Loa Revealed: Structure, Composition, History, and Hazards*, pp. 241–262, AGU, Washington, D. C., doi:10.1029/GM092p0241.
Richter, F. M., A. M. Davis, D. J. DePaolo, and E. B. Watson (2003), Isotope fractionation by chemical diffusion between molten basalt and rhyolite, *Geochim. Cosmochim. Acta*, *67*(20), 3905–3923, doi:10.1016/S0016-7037(03)00174-1.
Rondon, L., O. Pouliquen, and P. Aussillous (2011), Granular collapse in a fluid: Role of the initial volume fraction, *Phys. Fluids*, *23*(7), 073301, doi:10.1063/1.3594200.
Rothenburg, L., and R. J. Bathurst (1989), Analytical study of induced anisotropy in idealized granular materials, *Géotechnique*, *39*(4), 601–614, doi:10.1680/geot.1989.39.4.601.
Rothenburg, L., and R. J. Bathurst (1993), Influence of particle eccentricity on micromechanical behavior of granular materials, *Mech. Mater.*, *16*(1), 141–152, doi:10.1016/0167-6636(93)90037-R.
Royer, J. R., D. L. Blair, and S. D. Hudson (2016), Rheological signature of frictional interactions in shear thickening suspensions, *Phys. Rev. Lett.*, *116*(18), 188301, doi:10.1103/PhysRevLett.116.188301.
Rubin, A. E., K. M. Cooper, C. B. Till, A. J. R. Kent, F. Costa, M. Bose, D. Gravley, C. D. Deering, and J. W. Cole (2017), Rapid cooling and cold storage in a silicic magma reservoir recorded in individual crystals, *Science*, *356*(6343), 1154–1156, doi:10.1126/science.aam8720.
Ruprecht, P., G. W. Bergantz, K. M. Cooper, and W. Hildreth (2012), The crustal magma storage system of Volcán Quizapu, Chile, and the effects of magma mixing on magma diversity, *J. Petrol.*, *53*(4), 801–840, doi:10.1093/petrology/egs002.
Rutherford, M. J. (2008), Magma ascent rates, *Rev. Mineral. Geochem.*, *69*(1), 241–271, doi:10.2138/rmg.2008.69.7.
Saar, M. O., M. Manga, K. V. Cashman, and S. Fremouw (2001), Numerical models of the onset of yield strength in crystal–melt suspensions, *Earth Planet. Sci. Lett.*, *187*(3), 367–379, doi:10.1016/S0012-821X(01)00289-8.
Satake, M., and S. C. Cowin (1978), Constitution of mechanics of granular materials through the graph theory, in *Proceedings of U.S.-Japan Seminar on Continuum Mechanical and Statistical Approaches in the Mechanics of Granular Materials*, edited by S. C. Cowin and M. Satake, pp. 47–62, Gakujutsu Bunken Fukyu-Kai, Tokyo.
Sawyer, E. W. (2008), *Atlas of Migmatites*, 387 pp., NRC Res.h Press and Mineral. Assoc. of Canada, Ottawa, doi:10.1139/9780660197876.
Schleicher, J. M., G. W. Bergantz, R. E. Breidenthal, and A. Burgisser (2016), Time scales of crystal mixing in magma mushes, *Geophys. Res. Lett.*, *43*, 1543–1550, doi:10.1002/2015GL067372.
Schmidt, M. W., M. Forien, G. Solferino, and N. Bagdassarov (2012), Settling and compaction of olivine in basaltic magmas: An experimental study on the time scales of cumulate formation, *Contrib. Mineral. Petrol.*, *164*(6), 959–976, doi:10.1007/s00410-012-0782-0.
Siemens, A. O. N., and M. van Hecke (2010), Jamming: A simple introduction, *Physica A: Stat. Mech. Appl.*, *389*(20), 4255–4264, doi:10.1016/j.physa.2010.02.027.
Silbert, L. E. (2010), Jamming of frictional spheres and random loose packing, *Soft Matter*, *6*(13), 2918–2924, doi:10.1039/C001973A.
Sinton, J. M., and R. Detrick (1992), Mid-ocean ridge magma chambers, *J. Geophys. Res.*, *97*, 197–216, doi:10.1029/91JB02508.
Smith, W. O., P. D. Foote, and P. F. Busang (1929), Packing of homogeneous spheres, *Phys. Rev.*, *34*(9), 1271–1274.
Solgadi, F., and E. W. Sawyer (2008), Formation of igneous layering in granodiorite by gravity flow: A field, microstructure and geochemical study of the Tuolumne Intrusive Suite at Sawmill Canyon, California, *J. Petrol.*, *49*(11), 2009–2042, doi:10.1093/petrology/egn056.
Song, C., P. Wang, and H. A. Makse (2008), A phase diagram for jammed matter, *Nature*, *453*(7195), 629–632.
Souzy, M., P. Pham, and B. Metzger (2016), Taylor's experiment in a periodically sheared particulate suspension, *Phys. Rev. Fluids*, *1*(4), 042001.
Sperl, M. (2006), Experiments on corn pressure in silo cells—Translation and comment of Janssen's paper from 1895, *Granul. Matter*, *8*(2), 59–65, doi:10.1007/s10035-005-0224-z.
Stachowiak, G., and A. Batchlor (2013), *Engineering Tribology*, Butterworth-Heinemann, Amsterdam.
Staron, L., P.-Y. Lagrée, C. Josserand, and D. Lhuillier (2010), Flow and jamming of a two-dimensional granular bed: Toward a nonlocal rheology?, *Phys. Fluids*, *22*(11), 113303, doi:10.1063/1.3499353.
Stelten, M. E., K. M. Cooper, J. B. Wimpenny, J. A. Vazquez, and Q.-Z. Yin (2017), The role of mantle-derived magmas in the isotopic evolution of Yellowstone's magmatic system, *Geochem. Geophys. Geosyst.*, *18*, 1350–1365, doi:10.1002/2016GC006664.
Terzaghi, K. (1920), Old earth-pressure theories and new test results, *Engineering News-Record*, *85*(14), 632–637.
Thomson, A., and J. Maclennan (2013), The distribution of olivine compositions in Icelandic basalts and picrites, *J. Petrol.*, *54*(4), 745–768, doi:10.1093/petrology/egs083.
Tordesillas, A. (2007), Force chain buckling, unjamming transitions and shear banding in dense granular assemblies, *Phil. Magazine*, *87*(32), 4987–5016, doi:10.1080/14786430701594848.
Tordesillas, A., J. Zhang, and R. Behringer (2009), Buckling force chains in dense granular assemblies: Physical and numerical experiments, *Geomech. Geoeng.*, *4*(1), 3–16, doi:10.1080/17486020902767347.
Tordesillas, A., C. A. H. Steer, and D. M. Walker (2014), Force chain and contact cycle evolution in a dense granular material under shallow penetration, *Nonlin. Processes Geophys.*, *21*(2), 505–519, doi:10.5194/npg-21-505-2014.

Truesdell, C. A. (1980), The nature and function of constitutive relations, in *EPRI Workshop Proceedings: Basic Two-Phase Flow Modelling in Reactor Safety and Performance*, edited by Y. Zvirin, pp. 41–44, Electric Power Research Institute, Palo Alto.

Trulsson, M., B. Andreotti, and P. Claudin (2012), Transition from the viscous to inertial regime in dense suspensions, *Phys. Rev. Lett.*, *109*(11), 5, doi:10.1103/PhysRevLett.109.118305.

Tsuji, Y., T. Kawaguchi, and T. Tanaka (1993), Discrete particle simulation of two-dimensional fluidized bed, *Powder Technol.*, *77*(1), 79–87, doi:10.1016/0032-5910(93)85010-7.

van Hecke, M. (2010), Jamming of soft particles: Geometry, mechanics, scaling and isostaticity, *J. Phys. Condens. Matter*, *22*(3), 033101.

Vanel, L., D. Howell, D. Clark, R. P. Behringer, and E. Clément (1999), Memories in sand: Experimental tests of construction history on stress distributions under sandpiles, *Phys. Rev. E*, *60*(5), R5040–R5043.

Vermeer, P. A., W. Ehlers, H. J. Hermann, and E. Ramm (Eds.) (2004), *Modelling of Cohesive-Frictional Materials: Proceedings of Second International Symposium on Continuous and Discontinuous Modelling of Cohesive-Frictional Materials (CDM 2004)*, 446 pp., CRC Press, Boca Raton, Fla.

Vitelli, V., and M. van Hecke (2011), Soft materials: Marginal matters, *Nature*, *480*(7377), 325–326.

Waitukaitis, S. R., and H. M. Jaeger (2012), Impact-activated solidification of dense suspensions via dynamic jamming fronts, *Nature*, *487*(7406), 205–209.

Wakabayashi, T. (1950), Photo-elastic method for determination of stress in powdered mass, *J. Phys. Soc. Japan*, *5*(5), 383–385.

Walker, B. A., G. W. Bergantz, J. E. Otamendi, M. N. Ducea, and E. A. Cristofolini (2015), A MASH zone revealed: The mafic complex of the Sierra Valle Fértil, *J. Petrol.*, *56*(9), 1863–1896, doi:10.1093/petrology/egv057.

Walker, G. P. L. (1999), Volcanic rift zones and their intrusion swarms, *J. Volcanol. Geotherm. Res.*, *94*(1), 21–34, doi:10.1016/S0377-0273(99)00096-7.

Wallace, G. S., and G. W. Bergantz (2005), Reconciling heterogeneity in crystal zoning data: An application of shared characteristic diagrams at Chaos Crags, Lassen volcanic center, California, *Contrib. Mineral. Petrol.*, *149*, 98–112.

Wambaugh, J. F. (2010), Simple models for granular force networks, *Physica D: Non. Phen.*, *239*(18), 1818–1826, doi:10.1016/j.physd.2010.06.005.

Ward, K. M., G. Zandt, S. L. Beck, D. H. Christensen, and H. McFarlin (2014), Seismic imaging of the magmatic underpinnings beneath the Altiplano-Puna volcanic complex from the joint inversion of surface wave dispersion and receiver functions, *Earth Planet. Sci. Lett.*, *404*, 43–53, doi:10.1016/j.epsl.2014.07.022.

Wildemuth, C. R., and M. C. Williams (1984), Viscosity of suspensions modeled with a shear-dependent maximum packing fraction, *Rheol. Acta*, *23*, 627–635.

Wildemuth, C. R., and M. C. Williams (1985), A new interpretation of viscosity and yield stress in dense slurries: Coal and other irregular particles, *Rheol. Acta*, *24*, 75–91.

Wroth, C. P. (1958), Soil behaviour during shear—Existence of critical void ratios, *Engineering*, *186*(4829), 409–413.

Wyart, M., and M. E. Cates (2014), Discontinuous shear thickening without inertia in dense non-Brownian suspensions, *Phys. Rev. Lett.*, *112*(9), 098302.

Yamamoto, S., and T. Matsuoka (1997), Dynamic simulation of a platelike particle dispersed system, *J. Chem. Phys.*, *107*(8), 3300–3308, doi:10.1063/1.474681.

Yang, F.-L., and M. L. Hunt (2006), Dynamics of particle-particle collisions in a viscous liquid, *Phys. Fluids*, *18*(12), doi:10.1063/1.2396925.

Zhang, Q., and K. Kamrin (2017), Microscopic description of the granular fluidity field in nonlocal flow modeling, *Phys. Rev. Lett.*, *118*(5), 058001.

Zhao, J., and N. Guo (2015), The interplay between anisotropy and strain localisation in granular soils: A multiscale insight, *Géotechnique*, *65*(8), 642–656, doi:10.1680/geot.14.P.184.

Zhong, W., A. Yu, X. Liu, Z. Tong, and H. Zhang (2016), DEM/CFD-DEM modelling of non-spherical particulate systems: Theoretical developments and applications, *Powder Technol.*, *302*, 108–152, doi:10.1016/j.powtec.2016.07.010.

Journal of Geophysical Research: Solid Earth

Supporting Information for

On the kinematics and dynamics of crystal-rich systems

George W. Bergantz[1], Jillian M. Schleicher[1], Alain Burgisser[2]

[1] Department of Earth and Space Sciences, Box 351310, University of Washington, Seattle, WA 98195 USA

[2] Institut des Sciences de la Terre, CNRS – IRD – Université de Savoie, Campus Scientifique, 73376 Le Bourget du Lac, France

Introduction

This supplementary text provides details of the simulation methods, which include the model theory and governing equations, simulation initialization, and code validation. It also includes details of the supplementary movie file.

Text S1. Simulation Methods

Multiphase fluid simulation theory and algorithm

We performed simulations using a modified version of the MFIX (Multiphase Flow with Interphase eXchange) numerical algorithm developed by the Department of Energy supported National Energy and Technology Laboratory. It simulates multiphase flow by employing discrete element method-computational fluid dynamics (DEM-CFD). This is a Lagrangian-Eulerian approach for solid (crystal) and fluid (liquid) phases, respectively, where the center of mass of crystal phases are explicitly resolved and the liquid phase is treated as a continuum. This method allows us to model crystal-crystal and hydrodynamic interactions, that is, 4-way coupling. Collisions, sustained frictional contact, buoyancy, fluid drag and interphase momentum transport between phases are directly resolved with the soft-sphere approach, using a spring-dashpot system to model

the contact forces [*Cundall and Strack*, 1979]. The MFIX DEM-CFD algorithm has been verified and validated [*Garg et al.*, 2012a; b; *Li et al.*, 2012] including the physical effects of chemical reactions [*Li and Guenther*, 2012]; validation is discussed in detail below. Our simulations were run on the Stampede Cluster at the Texas Advanced Computing Center (TACC).

Governing Equations

The liquid phase is described with the governing equations for mass and momentum conservation:

$$\frac{\partial \varepsilon_l \rho_l}{\partial t} + \nabla \cdot \left(\varepsilon_l \rho_l \mathbf{v}_l \right) = 0 \tag{1}$$

$$\frac{D}{Dt}\left(\varepsilon_l \rho_l \mathbf{v}_l \right) = \nabla \cdot \overline{\overline{S}}_l + \varepsilon_l \rho_l \mathbf{g} - \mathbf{I}_{lc} \tag{2}$$

Here, ε_l is the volume fraction of the liquid phase, ρ_l is the liquid density, $\mathbf{v}_l$ is the liquid phase velocity vector, $\mathbf{g}$ is the gravitational acceleration, $\mathbf{I}_{lc}$ is a coupling term that involves the transfer of momentum between the liquid and crystal phases, and $\overline{\overline{S}}_l$ is the liquid-phase stress-tensor, given by:

$$\overline{\overline{S}}_l = - P_l \overline{\overline{I}} + \overline{\overline{t}}_l \tag{3}$$

$$\overline{\overline{\tau}}_l = 2\eta_l \overline{\overline{D}}_l + \lambda_l tr(\overline{\overline{D}}_l)\overline{\overline{I}} \tag{4}$$

$$\overline{\overline{D}}_l = \frac{1}{2}\left[\nabla \mathbf{v}_l + \left(\nabla \mathbf{v}_l \right)^{\mathrm{T}} \right] \tag{5}$$

P_l is the liquid-phase pressure, $\overline{\overline{I}}$ is the identity matrix, and $\overline{\overline{t}}_l$ is the liquid-phase shear stress tensor. η_l and λ_l are the dynamic viscosity and second coefficient of viscosity for the liquid phase, and $\overline{\overline{D}}_l$ is the strain rate tensor.

An advection-diffusion equation is employed to model transport of a scalar attached to the liquid phase. This scalar acts as an inert tracer of a compositional field associated with new magma and is shared by mixing between the resident and incoming liquids:

$$\frac{\partial}{\partial t}\left(\varepsilon_l \rho_l C_l \right) + \nabla \cdot \left(\varepsilon_l \rho_l \mathbf{v}_l C_l \right) = \nabla \cdot \left(D_l \nabla C_l \right) \tag{6}$$

Here C_l is the concentration of the liquid scalar and D_l is the diffusion coefficient for the scalar in the liquid phase. The cation diffusivity in basaltic melts is typically of order 10^{-10} m^2/s [*Richter et al.*, 2003]. This produces a scalar Peclet number of at least order 10^5 for the most active regions of flow for the duration of the simulations. Therefore, the scalar diffusivity was set to zero with no noticeable change in the scalar field. Hence modeled variations in the scalar field are entirely due to advective mixing and numerical diffusion. We did not quantify the effects of numerical diffusion on scalar mixing.

The crystals in the simulation are Lagrangian particles, with coupled equations solved for individual crystals at each time step. The position of the crystals and their linear and angular momentum are calculated according to Newton's Laws:

$$\frac{d\mathbf{X}^{(i)}(t)}{dt} = \mathbf{V}^{(i)}(t) \tag{7}$$

$$m^{(i)} \frac{d\mathbf{V}^{(i)}(t)}{dt} = \mathbf{F}_T^{(i)}(t) = m^{(i)}\mathbf{g} + \mathbf{F}_d^{(i\hat{l}\,k)}(t) + \mathbf{F}_c^{(i)}(t) \tag{8}$$

$$I^{(i)} \frac{d\boldsymbol{\omega}^{(i)}(t)}{dt} = \mathbf{T}^{(i)}(t) \tag{9}$$

The superscript (*i*) represents each crystal within the domain, $\mathbf{X}^{(i)}(t)$ is the crystal position, $\mathbf{V}^{(i)}(t)$ is the crystal linear velocity, and $m^{(i)}$ is the i^{th} crystal's mass. $\mathbf{F}_T^{(i)}(t)$ is the sum of the forces acting upon the i^{th} crystal, $\mathbf{F}_d^{(i\hat{l}\,k)}(t)$ is the total drag force on the i^{th} crystal in the k^{th} liquid cell, and $\mathbf{F}_c^{(i)}(t)$ is the contact force from interactions with other crystals. The equation for angular velocity, $\boldsymbol{\omega}^{(i)}(t)$, includes the i^{th} crystal's moment of inertia $I^{(i)} = \frac{m^{(i)} d_c^{(i)}}{10}$ and the sum of the torques $\mathbf{T}^{(i)}(t)$ acting on the i^{th} crystal.

Additional details of the implementation of the spring-and-dashpot model for calculating collisional forces used in MFIX can be found in the documentation of the MFIX-DEM algorithm [*Garg et al.*, 2012a]. The values of the crystal-crystal coefficient of friction, restitution, and spring constant required for DEM are 0.1, 0.1, and 10^5 kg/s^2, respectively. The sensitivity of model outcomes to the choice of DEM parameters depends on the dynamic regime considered [*Paulick et al.*, 2015] although it has been noted particle dynamics in fluidized beds are not very sensitive to the choice of DEM

contact parameters [*Tsuji et al.*, 1993]. The coefficients of friction (μ_f) for non-compacted, melt-saturated olivine crystals have never been measured. Hence we assessed the sensitivity of both the quasi-static and fully-fluidized model results to variations in contact friction from values of 0.03 to 0.5. Neither the quasi-static results, the formation of fluidized granular eddies, or the mixing characteristics changed significantly over this interval, so a value of 0.1 was used.

The value of the restitution coefficient (e) changes for collisions of particles in a viscous liquid, as shown by experimental results [*Yang and Hunt*, 2006]. The authors defined a parameter called the binary Stokes number for colliding particles in a viscous liquid:

$$St_B = \frac{m^* \left(U_1 - U_2\right)}{6\pi\eta_l (r_c^*)^2} \tag{10}$$

where $m^*=(1/m_1+1/m_2)^{-1}$ and $r_c^*=(1/r_1+1/r_2)^{-1}$ are the reduced mass and radius of the two particles in the collision, respectively, $(U_1 - U_2)$ is the relative approach velocity of the particles, and η_l is the fluid dynamic viscosity. The restitution coefficient of two colliding particles increases with increasing St_B. Our simulations generate $St_B << 1$, therefore based on the empirical data of particle-particle and particle-wall interaction in a viscous fluid the choice of $e = 0.1$ is appropriate [*Yang and Hunt*, 2006].

The values used for the particle stiffness coefficients (k_n, k_t) are approximately the same or a little lower than those of the natural geological materials, which can vary from $5x10^5$ to 10^6 Nm [*Cole and Hopkins*, 2016], because using the extreme end of actual values incurs simulation times that exceed any practical limits. However it has been shown in validation studies that reducing the particle stiffness coefficients (spring constants) does not produce measureable error, and this is common practice throughout the CFD-DEM community [*Nakamura and Watano*, 2007]. A DEM study [*Coetzee and Els*, 2009] demonstrated that particle stiffness coefficients below 10^5 kg/s^2 resulted in variable internal friction angle within the granular material. However, for k_n values at and above 10^5 kg/s^2 and low particle friction coefficients ($\mu_f < 0.2$), the angle of internal friction did not vary as a function of stiffness coefficient. We also performed a sensitivity study of the stiffness coefficients and found values that satisfy validation and do not give unrealistic compaction of the particle bed

Simulation initialization and properties

The simulations are 2.5-D, with the third dimension equaling the width of a crystal. Our simulation is for a dike-like body whose long dimension is into-and-out-of the plane of the domain, so 3-D edge effects are ignored and the liquid motion is governed by the quasi-2-D geometry. Accurate resolution of both the liquid and crystal dynamics requires that the liquid continuum grid-cell size has to be less than 1/19.3 of the domain size, and larger than 1.63 crystal diameters [*Peng et al.*, 2014]. We performed grid resolution studies and found that at a grid cell of 2.5 crystal diameters gave stable and reproducible results. The number of crystals is well above the minimum required to recover scalable, ensemble-averaged behavior [*Ness and Sun*, 2015].

The injection rate used in the simulation falls within the range of magma ascent rates of 10^{-4}-10^{1} m/s for volcanoes in a range of tectonic settings as estimated by geochemical, petrographic, and geophysical studies [*Girard and Stix*, 2009; *Parks et al.*, 2012; *Rutherford*, 2008]. Specifying the intrusion rate is appropriate for modeling open-system events driven by momentum, rather than by thermal or compositional buoyancy. This choice of input style is motived by the common occurrence of a complex crystal cargo in mixed magmas, with crystal clots, rapidly created disequilibrium features, and evidence for near instantaneous mingling of large volumes of magma [*Costa et al.*, 2010; *Davidson et al.*, 2001; *Wallace and Bergantz*, 2005], all of which indicate that many open-system events are strongly forced and can undergo mixing and mingling. In addition many open-system events have evidence that the open-system process has sufficient energy to overcome viscosity barriers producing mingled magmas with crystal transfer [*Ruprecht et al.*, 2012] as well as evidence of crystals transported out of a crystal mush which requires fluidization.

Solid boundaries have a no-slip boundary condition for the fluid and a wall-friction law for the crystals, but the majority of fluid and particle motion occurs far from the walls, so boundary conditions have little influence on the dynamics.

Code Validation

The validation of numerical models of dense multiphase mixtures is challenging. This is because granular-fluid mixtures are usually opaque, making optical measurements of laboratory experiments difficult. Inserting instruments into experimental systems would interfere with the flow field by particle-instrument interactions. In addition, the large number of degrees of freedom and many-body interactions produce emergent behavior, non-local and non-affine deformation such as shear-localization, dilatancy and jamming, all of which are not always repeated in duplicate experiments. Laboratory experiments can have multi-modal grain sizes with variable density and roughness, which is hard to duplicate in a numerical model for validation. Hence validation of numerical models for dense multiphase systems is usually based on the statistics of many realizations from an experimental test-bed that recovers the largest scales of the dynamics such as the global properties of mixing, pressure-drop, bed-height, or other measures of system-scale, granular ensemble behavior.

Numerous exercises have been previously performed on the MFIX-DEM code as validation studies [*Li and Guenther*, 2012]. This has included quasi-static granular flow such as run-out to reproduce the repose angle of glass beads, and under more dynamic conditions, simple multiphase shear flow, particle segregation and unmixing, as well as fully fluidized states. MFIX-DEM results and analog experiments gave very good agreement across the entire dynamic range. However we also developed validation exercises.

As our simulations exemplify a dynamic cycle from static to fully-fluidized, we must demonstrate validation for both these states. The Viscous number, I_v, and critical particle volume fraction, ϕ_{pc} ($\varepsilon_{c,c}$ in the nomenclature of the Supplementary Information), framework (defined in the main text) provide a basis for identifying which dynamic regime and validation protocols are appropriate [*Ness and Sun*, 2015]. The Viscous number is zero in the initial quasi-static regime where the volume fraction is near critical at the random packing of approximately 0.6. In the fully fluidized regime the Viscous number is variable with values spanning more than an order of magnitude and with a variable crystal volume fraction that is below the critical crystal volume fraction.

The validation of the initial quasi-static state where the mixing bowl is first formed was based on replicating the fluidization of granular soils [*Alizadeh et al.*, 2014]. Our model reproduced the same geometry and conditions as the analog experiments, indicating that our implementation of MFIX-DEM is recovering the quasi-static, viscoplastic, dense phase behavior. In this regime, crystal collisions are unimportant and are primarily frictional. Instead, sustained contact forces produce stress chains and the formation of bounding faults that create the mixing bowl. The formation of these bounding faults is followed by the Reynolds' dilatancy leading to the initiation of fluidization. Our simulations capture this process, in accord with experimental results [*Alizadeh et al.*, 2014].

After the initial quasi-static response that forms the mixing bowl, four time scales compete to control the subsequent fluidization: one associated with the shearing from the momentum flux, one associated with the relaxation time of the crystal-crystal contacts, one associated with the steady forcing of gravity, and one associated with the dissipation from liquid viscosity. For the values of the Viscous number from our simulations, which is never greater than unity, the fluidized portion of the system is always in a quasi-Newtonian regime. Direct validation for this regime is difficult to obtain as no existing experiments satisfied all the scaling requirements for verisimilitude. Alternatively, we invoke a previous MFIX-DEM validation exercise [*Li et al.*, 2012] of a bubbling fluidized bed as a proxy validation for our fluidized regime, as it has body forces and non-steady behavior. However it is in a more fluidized dynamic regime where the Viscous number is greater, and so the dissipation mechanisms are not going to be weighted the same as they are in our simulations. Nonetheless, that validation exercise, which may in fact be a more challenging validation test example than ours, produced excellent agreement with experiments. In summary, our implementation of MFIX-DEM code meets validation as far as can be determined from the existing analog experiments.

Calculations used in Figure 11:

To assess the situation of a mafic magma, we set η_f = 10 Pa s and d = 4 mm. For the felsic case, η_f = 10^4 Pa s and d = 1 mm. In both cases, $\Delta\rho$ = 600 kg/m^3, contact roughness is set to δ_{rough} = 1 μm, and ϕ_{RCP}=0.64.

We assessed convection at a single crystal content of $\phi = 0.5$, which implies that $\alpha = 1.25\times10^{-3}$. This choice increases the clarity of Fig. 11 because there is otherwise a large overlap between the I_{vP} and s values for convection and injection. At large Rayleigh number, Ra, and large Prandtl number, Pr, convective motions occur through unsteady structures such as viscous plumes. Estimating the shear rate occurring within these instabilities requires their characteristic width and velocity. We assume that the velocity of the Rayleigh-Taylor plumes, U_{RT}, can be estimated from the characteristic velocity entering into the large-scale Reynolds number, Re, which is related to Ra and Pr [*Grossmann and Lohse*, 2001] by:

$$Re = \frac{\rho_m U_{RT} H}{\eta_m} = 0.015 Ra^{2/3} Pr^{-1} \quad (11)$$

where H is the height of the convecting system, ρ_m and η_m are the fluid bulk density and viscosity, respectively. We assume next that the width of the Rayleigh-Taylor plumes, δ_{RT}, can be estimated thanks to the minimum spacing between the plumes (Fig. 10 of *Androvandi et al.* [2011]):

$$\delta_{RT} = 10^{5/3} H Ra^{1/3} \quad (12)$$

The characteristic convective shear rate is thus:

$$\dot{\gamma} = \frac{2U_{RT}}{\delta_{RT}} = 6.46\times10^{-4} \frac{\kappa}{H^2} Ra \quad (13)$$

where $\kappa = 10^{-6}$ m^2/s is the thermal diffusivity. We checked that Eqs (11-12) yield the correct orders of magnitude by comparing calculated and measured plume width and velocity of two experiments of *Androvandi et al.* [2011]. Calculated values for experiment IRa12 are U_{RT} = 1.7 mm/s and δ_{RT} = 18 mm, which is close to the respective measured values of ~ 2 mm/s and ~20 mm (Fig. 4 of *Androvandi et al.* [2011]). Calculated values for experiment syr3m are U_{RT} = 0.76 mm/s and δ_{RT} = 3.9 cm, which is close to the respective measured values of ~ 0.3 mm/s and ~5 cm (Fig. 6 of *Androvandi et al.* [2011]).

We varied H from 100 m to 2 km, and Ra within validity limit of this relationship ~10^4 to 10^9 and found that $10^{-12} < \dot{\gamma} < 10^{-4}$ 1/s. This range can be compared to the thermo-chemical modeling of *Petrelli et al.*[2016], who conducted numerical simulations of the

convection of a cooling magma body that starts from a high-temperature, crystal-free mafic magma and that ends when crystallization reaches ~80 vol.%. Using their model output for the pure buoyancy case, we find that strain rates range from 10^{-8} to 5.6 1/s at the beginning of the run when the convecting magma is mostly basaltic in composition. In the middle of the run when the convecting magma is mostly felsic, strain rates range from 10^{-8} to 10^{-4} 1/s. Considering that the high end of the basaltic strain rates of *Petrelli et al.* [2016] probably overestimates natural conditions because their simulation starts from a homogeneous, near liquidus magma body emplaced instantaneously in the crust, and that the low end of strain rates estimated using (13) yields extremely small I_{vP} and s values that cannot easily be shown at the scale of Fig. 11, we chose to consider that $10^{-8} < \dot{\gamma} < 10^{-2}$ 1/s for the felsic case and $10^{-8} < \dot{\gamma} < 1$ 1/s for the basaltic case.

The maximum confining pressure at the base of a mush can be estimated by the weight of the mush column:

$$P_{max} = \phi \Delta\rho g H F_{cf} \tag{14}$$

where F_{cf} is a factor that takes into account that some particles carry more than the average load because of contact forces. We maximize P_{max} by setting F_{cf} to 2.5, which implies that 40% of the particles carry all the bed weight (see discussion for Figure 5 in main text). This is a maximum value because load-bearing force chains carry more than the average load, but not all of it. Varying H from 100 m to 2 km and setting $\phi = 0.5$ and $\Delta\rho = 600$ kg/m^3 yields $0.7 < P_{max} < 15$ MPa. The upper bound of this range is a reasonable maximum because the maximum overpressure a chamber can sustain before relieving it by wall fracturing and dike propagation is 10 - 40 MPa [*Jellinek and DePaolo*, 2003]. The lower bound of pressure is found atop the mush. It is given by setting the bed height to two particle diameters, F_{cf} to one, and adding a 2/3 factor to be consistent the calculation of v_p in the main text:

$$P_{min} = \frac{4}{3} \Delta\rho g d \tag{15}$$

The minimum pressure is between 8 and 31 Pa for a rhyolite and a basalt, respectively.

We assessed mixing by reinjection at a range of crystal contents of $0.3 < \phi < 0.67$, which takes into account that mush remobilization implies some degree of dilution. The

framework of viscous and Sommerfeld numbers applies to dense systems and 30 vol% crystals is a maximum lower bound below which the lubrication force formulation we use is no longer valid [*Marzougui et al.*, 2015]. When assessing magma mixing, the injection velocity, v, below a mush pile during a reactivation event is difficult to constrain. The upper bound of v can be constrained by the low end of the range of magma ascent rates during eruption, which is $10^{-4} – 10^{1}$ m/s for volcanoes in a range of tectonic settings as estimated by geochemical, petrographic, and geophysical studies[*Girard and Stix*, 2009; *Parks et al.*, 2012; *Rutherford*, 2008]. It can also be constrained by the upper range of short-term magma recharge estimates from geophysical and thermal modeling, which is $10^{-3} – 1$ km^3/yr [*Caricchi et al.*, 2014; *Le Mével et al.*, 2016]. Assuming that the area of injection lies between 10 and 10^3 m^2, which corresponds either to a dyke of 1 m wide and $10 – 10^3$ m long, or to a distributed flow over 0.03 – 3% of a circular recharge area of 200 m in diameter, the upper range of magma recharge rates is $3\times10^{-5} – 3$ m/s. The minimum recharge rate can be constrained by the long-term, average flux of magma from depth, which is about 10 times lower than the short-term values [*Caricchi et al.*, 2014]. These constraints led us to consider injection velocities of $10^{-6} – 1$ m/s for the felsic case and $10^{-5} – 1$ m/s for the mafic case. The higher minimum value for the basalt case ensures that v is larger than the crystal settling velocity. The typical shear rate is given by:

$$v = \dot{\gamma} l \tag{16}$$

where l is the injection half-width. Considering typical dike widths [*Dufek and Bergantz*, 2005; *Walker*, 1999], we set l = 0.5-5 m. We consider that the mush pile is 1 to 100 m thick and estimate the bounds of confining pressure with (14-15).

To describe the field covered by Paterson experiments, we used that the working range of shear rates is $10^{-6} – 5\times10^{-3}$ 1/s, and particle size is usually ~100 μm [*Champallier et al.*, 2008; *Caricchi et al.*, 2008; *Forien et al.* 2011; *Pistone et al.*, 2012, 2015; *Okumura et al.*, 2015]. The upper bound of $\dot{\gamma}$ was adjusted by a representative multiplicative factor of 3.8 [*Forien et al.*, 2011] to take into account shear localization. Liquid viscosity spans from 10^5 to 10^{10} Pa s. It is generally varied jointly with crystal volume fraction [*Carrichi et al.*, 2008; *Champallier et al.*, 2008], so that the measured stress remains within the press sensitivity. The typical differential stress measured (or imposed by pore fluid pressure, *Okumura et al.*, [2016]) is 10-100 MPa. We use this

differential stress as a normal stress to calculate I_{vP} and s. It corresponds to assuming that s is dominated by the tangential lubrication forces, which has been shown in dense solid suspensions under simple shear [*Fernandez et al.*, 2013]. The pressure entering into I_{vP} is might be controlled by the confinement of the metal jacket surrounding the samples. As the jacket contribution generally amounts to 10% or less of the differential stress [e.g., *Champallier et al.*, 2008], we cannot exclude that the values of I_{vP} might be one order of magnitude above the estimates reported in Fig. 11. In *Okumura et al*. [2015], $10^{-3} < \dot{\gamma} < 10^{-4}$ 1/s, $\eta_f = 3\times10^8$ Pa s, $\phi = 0.45$, and $10 < d < 800$ μm (the lower bound is the median size by number and the upper bound is the median size by area). In *Forien et al.* [2011], $\dot{\gamma} = 2.3\times10^{-3}$ 1/s, $\eta_f = 2\times10^{10}$ Pa s, $\phi = 0.5$, and $d = 100$ μm.

Here we describe the field of analog experiments. In *Cimarelli et al.* [2011], the measured stress ranges from 25 to 500 Pa, $10^{-4} < \dot{\gamma} < 1$ 1/s, $\eta_f = 41$ Pa s, $\phi = 0.5$, and $50 < d < 250$ μm. In *Moitra et al.* [2015], the measured stress ranges from 0.01 to 6000 Pa, $10^{-4} < \dot{\gamma} < 10$ 1/s, $\eta_f = 102$ Pa s, and $4 < d < 122$ μm. Particle volume fraction varies from 0.1 to 0.6, but we here considered the high range $0.3 < \phi < 0.6$. In *Castruccio et al*. [2010], the basal differential pressure of the current ranges from 20 to 100 Pa, $2 < \eta_f < 80$ Pa s, and $0.1 < d < 1.5$ mm. Particle volume fraction varies from 0 to 0.67, but we here considered the high range $0.3 < \phi < 0.67$. The gravity current speed can be estimated from their Eq. (6), which yields $0.01 < v < 0.4$ m/s. Considering that current heights are $3 < H < 8$ cm, we get $0.13 < \dot{\gamma} < 13$ 1/s. In *Forien et al.* [2015], the shear stress at the base of the inclined flow pressure of the current ranges from 1 to 12 Pa, $\eta_f = 1.4$ Pa s, $10^{-5} < v < 10^{-3}$ m/s, $6\times10^{-4} < \dot{\gamma} < 0.1$ 1/s, $\phi = 0.6$, and $1 < d < 4$ mm.

Table S1. Model parameters for the DEM simulations

Parameter [units]	Variables	Values
Domain size [m]	x, y	2.56 x 1.28
Grid size [m]		0.01 x 0.01
Injection width [m]	I_w	0.32
Fluid density [kg/m^3]	ρ_f	2650
Fluid viscosity [Pa s]	η_f	0.2
Particle density [kg/m^3]	ρ_p	3300
Particle diameter [m]	d	0.004
Initial bed height [m]	H_0	0.823
Number of particles		147,040
Particle spring stiffness coefficient (normal and tangential) [kg/s^2]	k_n, k_t	10^5
Particle restitution coefficient	e_n	0.1
Particle coefficient of friction	μ_p	0.1
Time step (Initial, maximum) [s]	Δt	10^{-6}, 10^{-4}
Simulation time [s]	t	100
Injection velocities [m/s]	U_0	.023
Minimum fluidization velocity [m/s]	U_{mf}	0.00103

Movie ms01. Simulation of reintrusion of magma mush with normal forces

The simulation has two panels, the upper panel is a bed of identical olivine crystals (rainbow colored as an aid in visualization) in a reservoir of basaltic melt (black), that is intruded from below by new melt of the same composition but colored white. Mixing between resident and new melt will produce shades between black and white. The lower panel is the normal force network, color-coded with reference to the instantons average force. Once a particle becomes fully fluidized it will not appear in the lower panel as it has no normal force.